KU LEUVEN

FACULTEIT WETENSCHAPPEN

Study of Neutron-Deficient $^{202-205}$Fr Isotopes with Collinear Resonance Ionization Spectroscopy

Stijn DE SCHEPPER

Promotor: Prof. dr. G. Neyens
K.U. Leuven

Co-promotor: *Dr. T. E. Cocolios*
University of Manchester

Begeleider: I. Budincevic
K.U. Leuven

Proefschrift ingediend tot het
behalen van de graad van
Master of Science in de Fysica

Academiejaar 2012-2013

©Copyright by KU Leuven

Zonder voorafgaande schriftelijke toestemming van zowel de promotor(en) als de auteur(s) is overnemen, kopiëren, gebruiken of realiseren van deze uitgave of gedeelten ervan verboden. Voor aanvragen tot of informatie i.v.m. het overnemen en/of gebruik en/of realisatie van gedeelten uit deze publicatie, wendt u tot de KU Leuven, Faculteit Wetenschappen, Geel Huis, Kasteelpark Arenberg 11 bus 2100, 3001 Leuven (Heverlee), Telefoon +32 16 32 14 01.

Voorafgaande schriftelijke toestemming van de promotor(en) is eveneens vereist voor het aanwenden van de in dit afstudeerwerk beschreven (originele) methoden, producten, schakelingen en programma's voor industrieel of commercieel nut en voor de inzending van deze publicatie ter deelname aan wetenschappelijke prijzen of wedstrijden.

©Copyright by KU Leuven

Without written permission of the promotors and the authors it is forbidden to reproduce or adapt in any form or by any means any part of this publication. Requests for obtaining the right to reproduce or utilize parts of this publication should be addressed to KU Leuven, Faculteit Wetenschappen, Geel Huis, Kasteelpark Arenberg 11 bus 2100, 3001 Leuven (Heverlee), Telephone +32 16 32 14 01.

A written permission of the promotor is also required to use the methods, products, schematics and programs described in this work for industrial or commercial use, and for submitting this publication in scientific contests.

المنارة للاستشارات

www.manaraa.com

Preface

Scientists are always looking for a unified theory that can explain all observed phenomena, the so-called Grand Unified Theory. In physics we are however far from this goal. Some separate fields of physics even face difficulties in their own realm. In the case of the atomic nucleus, there is no one theory that can explain all phenomena in the whole nuclear landscape.

The model that is most intuitive and accessible is the Liquid Drop Model developed by Gamow and used by Lise Meitner [1] and Otto Hahn to explain nuclear fission. The nucleus is modeled as an incompressible fluid of nucleons. This model forms additionally the basis for the semi-empirical mass formula [2] and takes into consideration the fact that nuclear matter can deform. This deformation is either intrinsically present in the nucleus or caused by exciting the nuclear system. This deformation is the origin of nuclear fission. Against all expectations these fission fragments may be asymmetrically distributed, as the nuclei do not systematically split into two equal fragments. This asymmetry can be understood in the framework of a different model, the Nuclear Shell Model, where additional stabilising aspects are identified.

In the 1930s and 1940s it was noticed that nuclei with some particular number of protons and neutrons are more stable than others [3]. This discovery led Maria Goeppert Mayer to the development of the Nuclear Shell Model [4]. This is a model very similar to that of atomic electrons moving in the central potential of the atomic nucleus. The protons and neutrons move about in a potential created by all other protons and neutrons. This causes the nucleons to occupy discrete orbits, in a similar fashion as the discrete orbits in the atomic shell model. Theoretically this model of the nucleus is very difficult to treat [5, 6]. The fact that *all nucleons* influence the nuclear potential well creates a high level of complexity in the calculations. Furthermore, while the Coulomb force that governs the nucleus-electron interaction is well understood, the strong nuclear force that holds the nucleus together is not. Several attempts have been made, but no single description has been found valid for all mass regions in the nuclear chart. The Nuclear Shell Model remains however at this moment one of the most complete descriptions available for the atomic nucleus. It is very powerful near the identified closed shells, but breaks down away from those systems.

A possible extension is the Nilsson Model or Deformed Shell Model that predicts that the single-particle orbit energy levels will change when the nucleus assumes a specific deformation. This will influence the structure of the nucleus and in extreme cases can affect the actual magic numbers [7]. If the Shell Model with its extensions is to be tested at its limits, it is necessary to probe the more exotic nuclei far from the valley of stability. That is the subject of this thesis.

Experimental information on nuclear structure can be obtained from the ground state properties. In this thesis the nuclear moments of neutron-deficient francium isotopes ^{202}Fr, ^{203}Fr, ^{204}Fr, ^{205}Fr and some of their isomers will be discussed. The data are obtained using the new Collinear Resonance Ionization Spectroscopy beam line at ISOLDE, CERN.

In **chapter 1**, an overview will be given where these nuclei fit in current nuclear structure research, while in **chapter 2** a theoretical introduction is given to the observables which allow extraction of information on the nuclear structure. **Chapter 3** will discuss the new experimental approach that was necessary to study the exotic neutron-deficient francium isotopes. The data collection and the analysis procedure will be highlighted in **chapter 4**, while the new physics results will be presented in **chapter 5**. A discussion on the meaning of these results is the content of **chapter 6**. A conclusion and outlook towards future research is the subject of the **final chapter**.

Acknowledgement

Deze thesis is het einde van een reis die voor mij iets langer duurde dan gepland. Zonder de hulp van verschillende mensen had ik het einde niet gehaald. Ik wil die mensen dan ook even expliciet bedanken.

Ik dank mijn protomor professor Neyens voor de kans die ze me gegeven heeft om deze thesis te doen. Het was een geweldige ervaring waar ik enorm van genoten heb en die me ook heel veel bijleerde. Mijn co-promotor Dr. Thomas Cocolios dank ik voor de uitgebreide discussies en de feedback op mijn werk, alsook voor de tijd in CERN.

Natuurlijk mag ik de kantoorgenoten niet vergeten: Hanne, Marieke, Ivan en Ruben. Jullie gezelschap maakte hard werken draagbaar en vooral mogelijk (leve sociale controle!). Ruben en Ivan verdienen een extra bedanking voor de leuke tijden in CERN en de roadtrips.

I am also very grateful to Kieran, Kara, Tom and Ronald for there invaluable insights and the fun at CERN.

Bedankt mama en papa. Jullie verdienen misschien wel het meeste dank van iedereen hier vernoemd. Zonder jullie had ik er niet aan kunnen beginnen en was ik nooit zover geraakt.

Een thesisjaar is een zwaar jaar van veel werken en frustraties. Het helpt dan als je af en toe vanachter je pc kan komen en genieten van kinderlijke onbezorgdheid. Daarvoor zorgden Lien en Coby. Niet dat ze het zelf beseffen, maar ze fleuren ieders dag op.

Iris, jou bedank ik voor je steun en luisterend oor. Ik prijs me gelukkig dat ik steeds op je kan rekenen.

Samenvatting

Het doel van deze masterthesis is de studie van neutronarme $^{202-205}$Fr isotopen. Die isotopen bevinden zich in de lood-regio op de kernkaart, een regio die bewijzen vertoond van vormcoëxistentie. Dit is een fenomeen waarbij twee toestanden nabij in energie een andere vorm hebben. Voor dit werk beperken we ons tot de grondtoestand en laagliggende isomere toestanden. Vormcoëxistentie wordt veroorzaakt door indringertoestanden. Dit zijn eendeeltjes Schillenmodeltoestanden die door vervorming van de kern van energie veranderen en zo de orde binnen een schil verstoren.

In de neutronarme lood-regio is het $3s_{1/2}$ orbitaal de belangrijkste proton indringertoestand. Naarmate de kernen neutronarmer worden, zal de vervorming toenemen. Het $\pi 3s_{1/2}$ orbitaal zal stijgen in energie en in competitie treden met het $\pi 1h_{9/2}$ orbitaal en zal uiteindelijk zelfs de grondtoestand worden in de oneven-A bismuth (Z=83) isotopen. Dezelfde situatie wordt ook waargenomen in astatine (Z=85), maar de inversie van beide toestanden gebeurt hier eerder. Hetzelfde fenomeen wordt ook verwacht in francium (Z=87) maar dan nog eerder in ^{199}Fr. Hoewel het onmogelijk is om de momenten van zulke neutronarme isotopen te bestuderen met de huidige stand van de techniek, is het wel belangrijk om de momenten van de hele isotopenketen te bestuderen. Het belangrijkste neutron indringertoestand orbitaal is het $1i_{13/2}$ orbitaal. Als functie van vervorming door het dalende aantal neutronen in de keten, zal dit orbitaal stijgen in energie. Dit orbitaal geeft aanleiding tot het ontstaan van isomere toestanden door het grote verschil in spin met de omringende orbitalen en het verschil in pariteit.

Het magnetisch moment geeft informatie over de bevolking van eendeeltje Schillenmodeltoestanden en de ladingstraal geeft informatie over de evolutie van de vorm in een isotopenketen. Met behulp van het nieuwe Collineaire Resonante Ionisatie Spectroscopie experiment in ISOLDE, CERN, kunnen deze modelonafhankelijke observabelen bepaald worden aan de hand van de hyperfijninteracties tussen kern en atomaire elektronen. CRIS maakt het ook mogelijk om isomere toestanden selectief te ioniseren en als zuivere bundel naar een experiment te sturen. Dit werd gebruikt om via de vervalkarakteristieken de hyperfijnspectra te analyseren.

In de literatuur werden spins en configuraties voor de meeste isotopen voorgesteld

aan de hand van vervalstudies en systematiek. In dit werk worden de meeste resultaten uit de literatuur bevestigd. ^{203}Fr en ^{205}Fr hebben beide spin 9/2 en configuratie $1\mathrm{h}_{9/2}$, zoals verwacht. De hoge-spin isomere toestanden in ^{202}Fr en ^{204}Fr hebben een zuivere $\left[\pi 1h_{9/2} \otimes \nu 1i_{13/2}\right]_{10^-}$ configuratie. De tweede isomere toestand in ^{204}Fr heeft, zoals voorgesteld in de literatuur, een zuivere $\left[\pi 1h_{9/2} \otimes \nu 2f_{5/2}\right]_{7^+}$ configuratie.

In tegenstelling tot wat voorgesteld werd in de literatuur, hebben de grondtoestanden van ^{202}Fr en ^{204}Fr een configuratie die een mix is van $\left[\pi 1h_{9/2} \otimes \nu 3p_{3/2}\right]_{3^+}$ en $\left[\pi 1h_{9/2} \otimes \nu 2f_{5/2}\right]_{3^+}$, waarbij de eerste de dominante bijdrage levert.

De ladingstraal van francium vertoont een afwijking van de sferische trend in lood eerder dan in polonium. Dit kan bewijs zijn dat de extra protonen de kern sterker polariseren.

Uit het verschil in de ladingstralen van het (10^-) isomeer en de (3^+) grondtoestand volgt dat beide een andere vorm hebben. Dit is een voorbeeld van vormcoëxistentie.

Summary

The scope of this master's thesis is the study of neutron-deficient $^{202-205}$Fr isotopes. These isotopes are inside the neutron-deficient lead region, a region that has shown evidence of shape coexistence. For this thesis, this discussion is limited to the phenomenon where a low lying excited state has a different shape than the ground state. Shape coexistence is caused by intruder states. These are single-particle Shell Model states that are perturbed in energy due to the interaction with a deformed core.

In the neutron-deficient lead region the main proton intruder orbit is the $3\mathrm{s}_{1/2}$ orbit. When going towards more neutron-deficient isotopes, deformation increases. The $\pi 3s_{1/2}$ orbit will rise in energy and will eventually become the ground state in odd-A bismuth (Z=83) isotopes. It is also observed in odd-A astatine (Z=85) isotopes, already in less neutron-deficient nuclei. The same phenomenon is expected to be present francium (Z=87) isotopes already at ^{199}Fr. Although it is currently impossible to study the moments of such an exotic nucleus, it is important to characterize the evolution of nuclear structure in the francium chain towards more neutron-deficient isotopes. The main neutron intruder orbit is the $1\mathrm{i}_{13/2}$ orbit. Deformation drives this orbit to raise in energy. Due to the large spin-gap and the difference in parity with the other Shell Model orbits in this shell, this orbit is cause for long-lived excited states.

The nuclear observable of interest to study Shell Model states is the magnetic moment and characterization of the evolution of the nuclear shape can be done using charge radii. Using the newly developed Collinear Resonance Ionization Spectroscopy beam line these model-independent observables are extracted using the hyperfine interactions between atomic electrons and the nucleus. The observables are used to extract information on occupation of single-particle Shell Model orbits and on the deformation of the nuclei. Using CRIS it is also possible to selectively ionize pure isomeric beams. This way the decay characteristics are used to disentangle the hyperfine structure spectra.

Spins and configurations are already proposed in literature for $^{202-205}$Fr and their isomers, mainly based on decay systematics. In this work the results from literature are confirmed for most isotopes and isomers. ^{203}Fr and ^{205}Fr both have spin 9/2 and

configuration $\pi 1h_{9/2}$ as expected. The high-spin isomeric states in ^{202}Fr and ^{204}Fr have been confirmed to have a pure single-particle $\left[\pi 1h_{9/2} \otimes \nu 1i_{13/2}\right]_{10^-}$ configuration. The second isomeric state in ^{204}Fr was confirmed to have a pure single-particle $\left[\pi 1h_{9/2} \otimes \nu 2f_{5/2}\right]_{7^+}$ configuration.

In contrary to what was proposed for the ground states of ^{202}Fr and ^{204}Fr we find evidence that suggests that the configuration is an admixture of $\left[\pi 1h_{9/2} \otimes \nu 3p_{3/2}\right]_{3^+}$ and $\left[\pi 1h_{9/2} \otimes \nu 2f_{5/2}\right]_{3^+}$, where the former is the dominant contribution.

For the charge radii a departure from the spherical trend in Pb is observed earlier than the departure in Po. This could prove that adding protons to the nucleus polarizes the nucleus more strongly.

From the charge radii it can also be concluded that in ^{204}Fr the (3^+) ground state and the (10^-) have a different shape and are thus an example of shape coexistence.

Contents

List of Figures

List of Tables

Chapter 1

Physical motivation

As briefly mentioned in the preface, the Shell Model is currently the most complete model available in nuclear structure. Just like in atomic theory where the electrons move in a central potential created by the atomic nucleus, a nucleon can be modeled as moving in a central potential created by all other nucleons. This central potential then results in the nuclear Shell Model. The different orbits of the Shell Model in the lead region for protons and neutrons are shown in figure 1.1. The difference between proton and neutron orbits is caused by the Coulomb force, which is of course absent in neutrons.

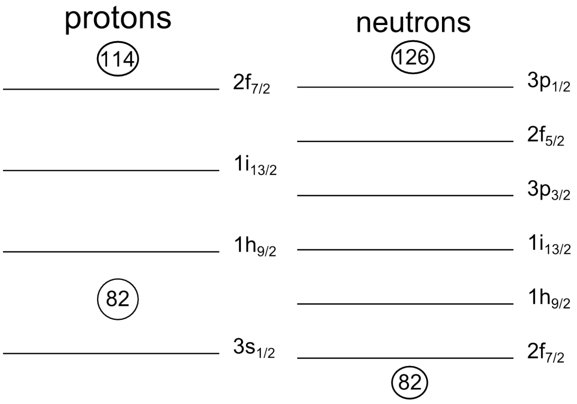

Figure 1.1: The Shell Model orbits for the lead region. The magic numbers of the shell closure are indicated.

The most stable nucleus in this region is ^{208}Pb, which has 82 protons and 126 neutrons. Neutron-deficient francium (Z=87) isotopes lie in the nuclear chart above this magic proton number Z=82 and below the magic neutron number N=126. The region in between these two magic numbers is known to present evidence of shape coexistence.

1.1 Shape coexistence

Shape coexistence is a phenomenon where discrete nuclear states within a narrow energy range may display various shapes, either spherical or deformed. For the interest of this thesis the discussion is limited to nuclear levels in the vicinity to the nuclear ground state. One mechanism which gives rise to shape coexistence is related to intruder states. An intruder state is a single-particle Shell Model orbit which is lowered in energy due to the interaction with the deformed core. Exciting a nucleon from its spherical orbit to the intruder state requires less energy than it would for excitation to another spherical orbit.

1.2 Even-even nucleus

A clear illustration of this effect is found in ^{186}Pb where two excited states with assumed completely different shapes have been found to exist within 700keV of the ground state [8]. These states are described to be the result of excitations to an oblate deformed 0^+ state, by exciting two protons to a higher orbit and leaving two holes in the original orbit (2p-2h), and a prolate deformed 0^+ state, by exciting 4 protons to a higher orbit and leaving 4 holes in the original orbit (4p-4h). Figure 1.2 shows the calculated potential energy surface as a function of deformation.

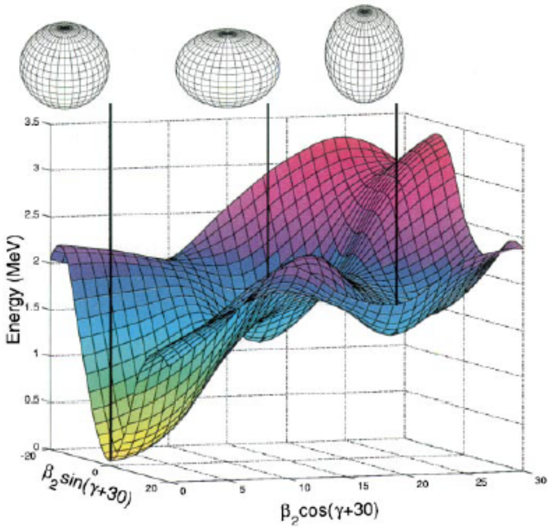

Figure 1.2: The calculated potential energy surface of ^{186}Pb as a function of deformation [8].

1.3 Odd-A nuclei

The addition of an unpaired proton or neutron has a large impact on the nuclear structure. In the single-particle Shell Model, this valence nucleon will be in a particular orbit and will, to a first order, determine the properties of the nucleus. In the extreme single-particle Shell Model, the nuclear spin can be a signature for the orbit occupied by the valence nucleon. The neutron and proton orbits in the region of interest are different and occupation of one or the other will therefore result in a different response from the nucleus.

1.3.1 Odd-Z nuclei

In neutron-deficient bismuth (Z=83) and thallium (Z=81) isotopes there is a coexistence of a $9/2^-$ state with a $1/2^+$ state as can be seen in figure 1.3. These states originate respectively from the single-particle proton $1h_{9/2}$ orbit and the proton $3s_{1/2}$ orbit as shown in figure 1.1. The $9/2^-$ state has a single proton (in Bi) or a hole (in Tl) in the $1h_{9/2}$ orbit and the $1/2^+$ state has a single proton (in Tl) or a hole (in Bi) in the $3s_{1/2}$ orbit. As you go down in neutron number from N=126, the excited state drops in energy. This evolution for thallium and bismuth is illustrated in figure 1.3. In thallium isotopes the $1/2^+$ state remains the ground state while the $9/2^-$ excited state reaches a minimum in energy at N=108. However in bismuth the $9/2^-$ ground state and the $1/2^+$ excited state undergo a quantum inversion as the $1/2^+$ state becomes the ground state.

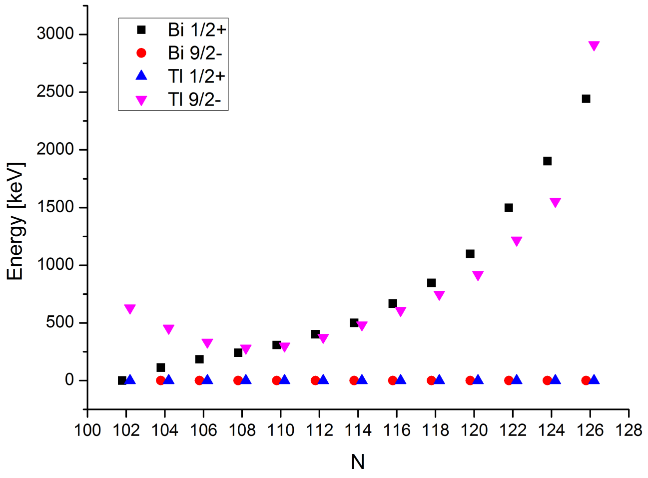

Figure 1.3: The evolution of the $9/2^-$ and $1/2^+$ states in bismuth and thallium [9].

Figure 1.4 shows the neutron number at which the inversion between the $9/2^-$ and $1/2^+$ state occurs for Bi and At. In bismuth it is seen at N=104, while for astatine (Z=85) it is seen at N=110. In francium (Z=87) it is expected to occur earlier at N=112[1]. The discrepancy between Z<82 and Z>82 is another illustration of the shell closure. The increasing neutron number at which the inversion occurs, suggests that adding protons more strongly polarizes the magic core of the nucleus and thus increases deformation for less neutrons, leading to a quicker inversion of the spherical and intruder orbit. For the isotopes of interest, ^{203,205}Fr, the ground state spins are expected to be $9/2^+$ [11, 12]. The $1/2^+$ state is observed in ^{205}Fr, but is not isomeric. In ^{203}Fr it is expected to be isomeric [13].

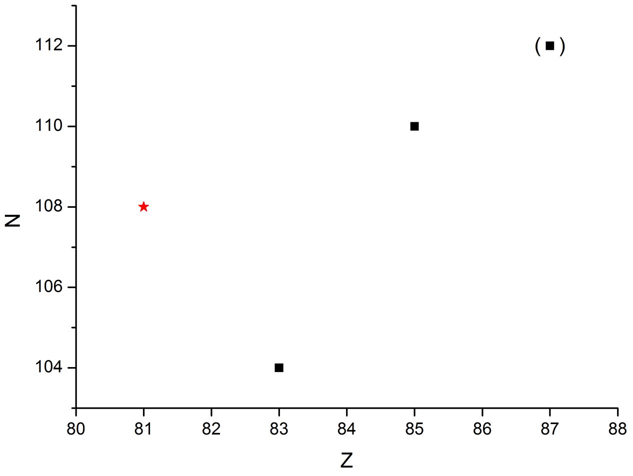

Figure 1.4: The neutron number at which the ground state and excited state are inverted as a function of proton number. For Z=81 the neutron number of minimum energy of the $9/2^+$ state is given, since there is no inversion present [9].

1.3.2 Odd-N nuclei

In the platinum isotopes (Z=78) deformation is different for the odd and the even isotopes. In odd platinum isotopes, the unpaired neutron favors axial symmetry, either oblate or prolate [14]. The even platinum isotopes show a transition from oblate shapes in the heavy nuclei to prolate in the light nuclei. The deformation is driven by the polarization of the soft platinum core by the intruder states. The difference in shape of the odd- and even-N isotopes is cause for an odd-even shape staggering in the charge radii (see figure 1.6). One of the most dramatic examples of shape staggering is found in the mercury (Z=80) isotopic chain where a large isomer

---

[1] Although recent data from SHIP (GSI) challenge the fact that the $1/2^+$ state becomes the ground state [10].

shift is observed in ^{185}Hg and a large odd-even staggering remains down to ^{181}Hg [15], as shown in figure 1.6.

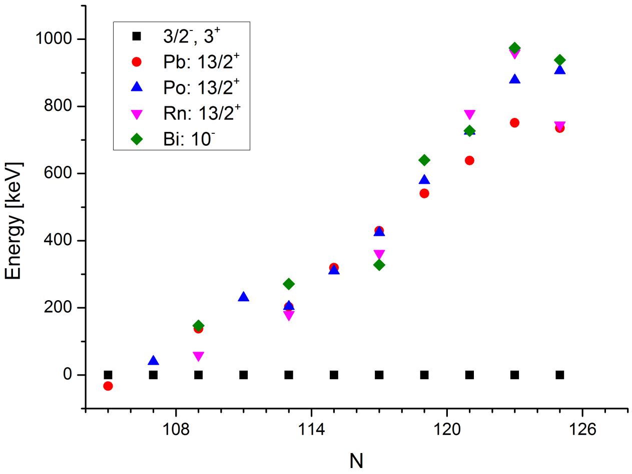

Figure 1.5: The even-Z $13/2^+$ state energy systematics of the compared to the energy systematics of the 10^- state in odd-odd nuclei [9]. All energies are normalized to the $3/2^-$ state in even-Z and 3^+ in odd-odd bismuth, which are not always the ground states.

Similarly to the $1h_{9/2}$-$3s_{1/2}$ duality in odd-Z nuclei, the neutron-deficient odd-N nuclei are the subject of a low-spin/high-spin competition between the neutron $1i_{13/2}$ and $2p_{3/2}$ orbits. Their relative evolution can be seen in figure 1.5. The proximity of those quantum levels with large spin difference, together with the limited quantum level density, results in a large numbers of isomers. It is also shown that these isomers have different deformation compared to the ground state [15]. For example the ground state in ^{187}Hg has a quadrupole moment of -0.75eb while the $13/2^+$ isomer has a quadrupole moment of +0.5eb.

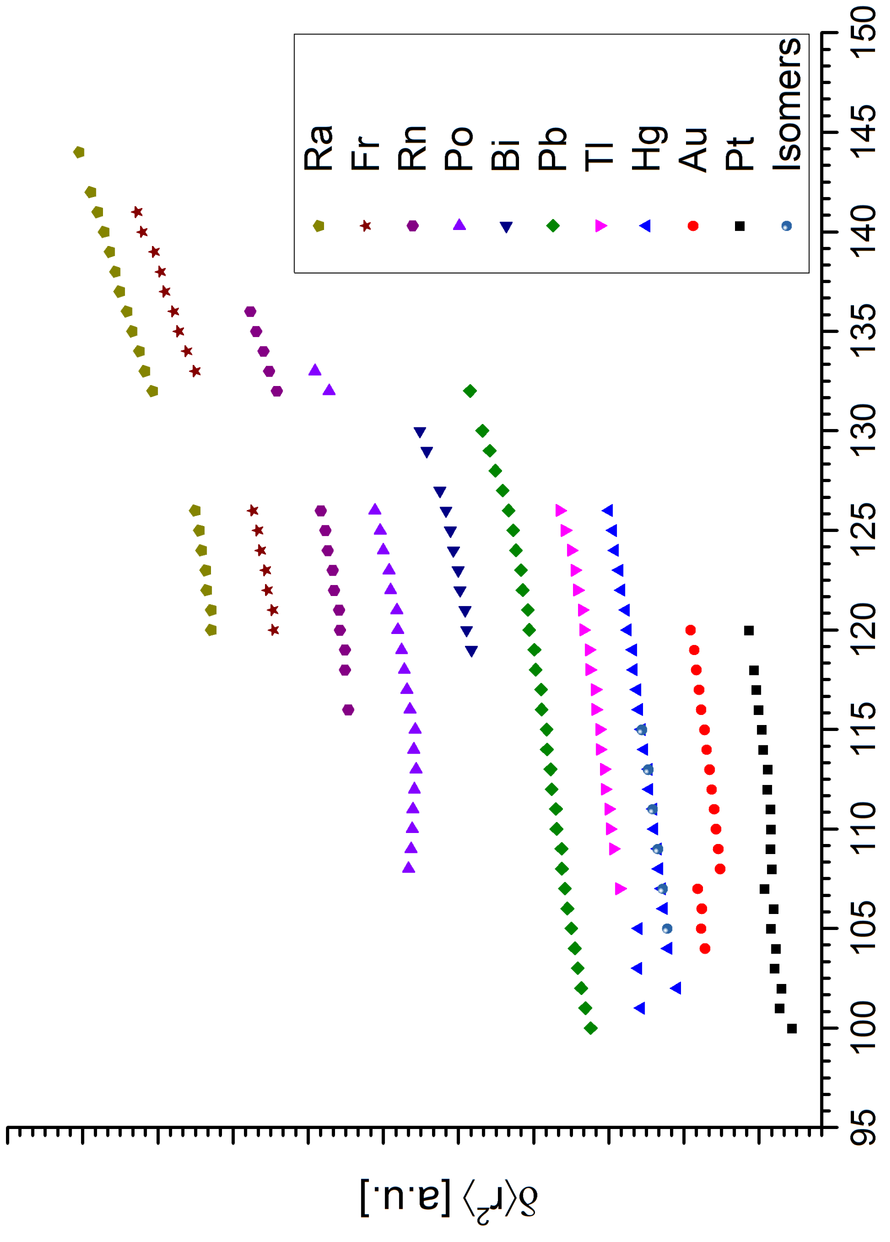

Figure 1.6: The change in charge-radii around Z=82 [16, 17, 15].

1.4 Odd-odd nuclei

The odd valence nucleons can couple in a diverse number of ways and it becomes increasingly difficult to predict the final outcome. In the odd-odd bismuth and thallium nuclei a wide range of long-lived isomeric states are found close in energy to the ground state.

Van Duppen et al [18] showed that in neutron-deficient thallium and bismuth (3^+) and (10^-) states are competing at low energy. The ground state of $^{194-198}$Bi alpha decays unhindered to the (3^+) state in the daughter thallium isotopes, hereby suggesting those two states have the same spin, parity and configuration. The (3^+) state is proposed to be the result of coupling of $\left[\pi 1h_{9/2} \otimes \nu 2f_{5/2}\right]$ or $\left[\pi 1h_{9/2} \otimes \nu 3p_{3/2}\right]$. The (10^-) state is present as an isomer in both neutron-deficient bismuth and thallium. The (10^-) isomer in bismuth decays to the (10^-) isomer in thallium by unhindered alpha decay as well. Both are proposed to be the result of the coupling of $\left[\pi 1h_{9/2} \otimes \nu 1i_{13/2}\right]$. The systematics of the (10^-) energy levels are compared to that of the even-Z $13/2^+$ systematics in figure 1.5.

Later Huyse et al [19] extended these results to astatine and francium. They observed very similar unhindered alpha decay chains from francium to astatine to bismuth. In ^{204}Fr and ^{202}Fr the ground state decays unhindered to the ground state in the astatine daughter. The astatine daughters again decay to the (3^+) ground state in the corresponding bismuth granddaughters. In all three generations the same unhindered sequence is observed for the (10^-) isomers. The configurations of these high and low spin states are based on the unhindered alpha decay chains to end eventually in thallium. Huyse et al [19] proposed that all (3^+) states are resulting from odd-odd coupling of $\left[\pi 1h_{9/2} \otimes \nu 2f_{5/2}\right]$.

In ^{204}Fr an additional isomer is present. It was proposed to be the result of a similar configuration as the (3^+) ground state, but with a different quantum alignment between the two nucleons. However due to the difference in spin, gamma decay from the (7^+) state to the (3^+) ground state is highly suppressed and the (7^+) state is isomeric. There was however a gamma transition observed in bismuth and astatine from the (10^-) isomer to the (7^+) isomer allowing the determination of its excitation energy [20]. The similarity in the evolution of the gamma energy as a function of neutron number with the $\nu i_{13/2}$ to $\nu f_{7/2}$ transition in neutron-deficient lead isotopes strengthened the argument for the proposed configurations. A summarized decay scheme for the decay chains in ^{202}Fr and ^{204}Fr are shown in figure 1.7 and 1.8.

By measuring the magnetic moments of $^{202-205}$Fr, we aim at gaining information on the configuration, while the changes in mean square charge radii provide information on the changes in shape of those nuclei and their isomers.

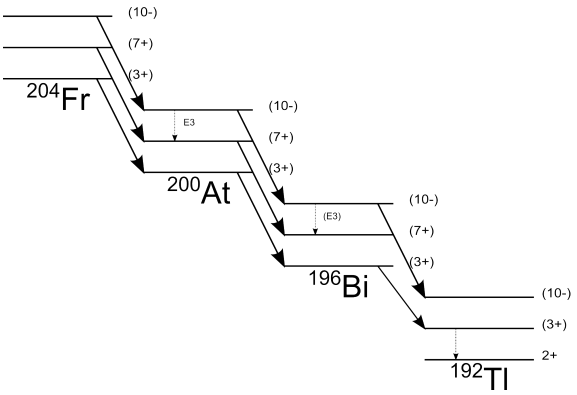

Figure 1.7: The alpha decay chain for ^{204}Fr, summarized from Van Duppen et al [18] and Huyse et al [19].

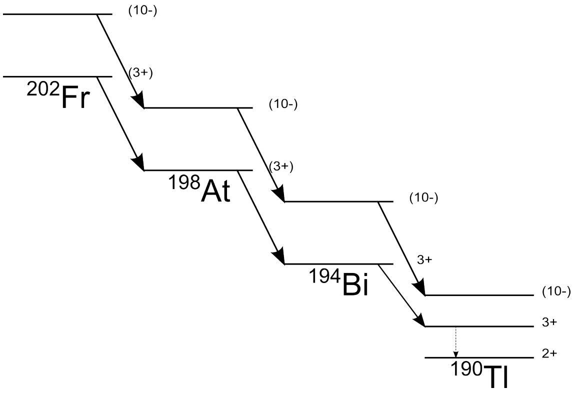

Figure 1.8: The alpha decay chain for 202Fr, summarized from Van Duppen et al [18] and Huyse et al [19].

Chapter 2

Nuclear moments

Although the nucleus is a composite body, it may be seen in many respects as a single unit with a quantum spin and nuclear moments. Those observables can be determined from the perturbation the nucleus induces on the atomic energy levels [21].

2.1 Nuclear spin

The quantum spin of the nucleus is determined by coupling together the angular momenta of all its constituents according to the orbits occupied by the nucleons. Most of those nucleons will however couple in pairs with spin 0, especially if an orbit is filled. The nuclear spin is then determined solely from the coupling of the remaining unpaired nucleons, called valence nucleons. This is best illustrated in the extreme single-particle Shell Model, where the properties of the nucleus are determined by one (odd-A) or two (odd-Z, odd-N) nucleons.

The situation in most nuclei is however more complicated. All nucleons above a filled orbit couple with one another and can couple in different ways. The proton-neutron coupling results in leading (second) order in a parabolic behavior of the energy distribution of states within a multiplet. This distribution is described by Paar [22] as a consequence of coupling of clusters of nucleons to phonons. This way it is possible to predict ground state spins of odd-odd nuclei near magic shells.

2.2 Isotope shift

The atomic nucleus is, to first order, assumed to be point-like It has however a finite size and shape. The mass and the volume of an element vary when changing the number of neutrons from its nucleus, or by changing its quantum configuration (isomers). The effect on the electronic energy levels, and consequently on atomic transitions, is a perturbation of the order of 1:1000000. With modern techniques, those perturbations have become measurable and can be described in terms of a mass shift and a field shift [23].

$$\delta\nu = \text{mass shift} + \text{field shift}$$

Because a point nucleus does not exist it is impossible to measure this shift absolutely. Instead, we can study the change in that shift with respect to a reference isotope:

$$\delta^{AA'} = \delta\nu_m^{AA'} + \delta\nu_f^{AA'} \tag{2.1}$$

Changing the number of neutrons in a nucleus will change the center of mass of the atomic system. This will induce a shift in the energy of the atomic levels of interest (normal mass shift). Because correlations between electrons are slightly different in different electronic configurations, there is also a level-dependent shift (specific mass shift). While the former can be exactly determined, the latter is too complex to be solved exactly for more than three electrons. The resulting shift scales as $\frac{1}{A^2}$ and is large for low mass nuclei and small for high mass nuclei. The mass shift is determined using accurate masses from direct mass measurements [24].

$$\delta\nu_m^{AA'} = M\frac{A' - A}{AA'},$$

where $\mathrm{M{=}K_{NMS}{+}K_{SMS}}$ is the mass factor, which is transition dependent.

The nucleus has a finite charge distribution and this also causes the atomic levels to shift. This shift is called the field shift and it is proportional to the change in the mean square charge radius between two isotopes. The charge radius is affected directly by the nuclear structure, such as by deformation and shell effects. A chain of isotopes is studied and aberrations from a trend can be considered as a manifestation of a change in nuclear structure.

$$\delta\nu_f^{AA'} = F\delta\langle r^2\rangle^{AA'},$$

where F is the field shift factor, which is also transition dependent, and $\delta\langle r^2\rangle^{AA'}$ is the change in charge radius.

The isotope shift thus equals

$$\delta\nu^{AA'} = M\frac{A' - A}{AA'} + F\delta\langle r^2\rangle^{AA'} \tag{2.2}$$

The nuclear quantity governing the isotope shift is the mean square charge radius:

$$\langle r^2\rangle = \frac{\int_0^R \rho\left(\boldsymbol{r}\right)\boldsymbol{r}^2 d\boldsymbol{r}}{\int_0^R \rho\left(\boldsymbol{r}\right) d\boldsymbol{r}} \tag{2.3}$$

For a liquid drop nucleus the mean square charge radius equals [21]

$$\langle r^2 \rangle_{LD} = \left(\frac{3}{5}\right) R^2 = \left(\frac{3}{5}\right) R_0^2 A^{2/3} \tag{2.4}$$

and for small deviations in A, this leads to

$$\delta \langle r^2 \rangle_{LD} = \left(\frac{2}{5}\right) R_0^2 A^{-1/3} \delta A. \tag{2.5}$$

Deviation from the trend set by eq. 2.5 reveals shell closures or changes in nuclear deformation. More over, an odd-even staggering can often be observed along a chain of isotopes.

The change in mean-square charge radius can be extracted from the isotope shift. This is dependent on the electronic transition that is used. Every transition has a different field shift factor, F_i, and mass shift factor, M_i. Since the difference in charge radius remains the same for two electronic transitions, it is possible to determine the field shift factor and the mass shift factor for a new transition by comparing the isotope shifts measured for reference isotopes with both transitions [25, 26].

$$\left(\frac{AA'}{A'-A}\delta\nu_j^{A,A'}\right) = \frac{F_j}{F_i}\left(\frac{AA'}{A'-A}\delta\nu_i^{A,A'}\right) + M_j - \frac{F_j}{F_i}M_i. \tag{2.6}$$

2.3 Magnetic dipole moment

Information on the occupation of particular orbits can also be acquired from the magnetic dipole moment of the nucleus. In the classical picture a magnetic dipole moment is caused by a current loop or by an orbiting charged particle. The nuclear orbits have angular momentum, so the protons, which are charged, in each orbit have an associated angular moment and thus a magnetic dipole moment. Classically the neutrons do not have a dipole moment, because of the lack of charge. However quantum mechanics assigns intrinsic magnetic moments to both protons and neutrons which is related to their intrinsic spin. The total magnetic dipole moment of the nucleus is a weighted sum of both contributions.

$$\mu = \sum_{i=1}^{A} g_l^i \mathbf{l}^i + \sum_{i=1}^{A} g_s^i \mathbf{s}^i \tag{2.7}$$

where g_l and g_s are the weights establishing the relative contribution of the intrinsic spin, s, and angular momentum, l, to the magnetic moment.

The magnetic dipole operator is an additive operator. This way it is possible to determine empirically the magnetic dipole moment of an odd-odd nucleus of spin J

with protons coupled to spin J_p and neutrons coupled to spin J_n [5] as follows:

$$\mu\left(J\right) = \frac{J}{2}\left[\frac{\mu\left(J_p\right)}{J_p} + \frac{\mu\left(J_n\right)}{J_n} + \left(\frac{\mu\left(J_p\right)}{J_p} - \frac{\mu\left(J_n\right)}{J_n}\right)\frac{J_p\left(J_p+1\right) - J_n\left(J_n+1\right)}{J\left(J+1\right)}\right] \tag{2.8}$$

The magnetic moment allows for a model-dependent confirmation of the valence nucleons orbital occupation. The model dependence is reflected in the change of magnetic moment of an orbit due to deformation or core polarization or excitation. In the case of Shell Model calculations, the extent of the model space can have a large impact on the predicted moment [27].

2.4 Quadrupole moment

The static deformation from a spherical shape can be derived from the electric quadrupole moment. This is the third term in the electric multipole expansion of the Coulomb interaction of the nucleus. The quadrupole moment operator is given by

$$\hat{Q} = \sum_{i=1}^{A} e_i\left(3z_i^2 - r_i^2\right).$$

Axially symmetric deformation from a spherical shape is classified as oblate or prolate, as shown in figure 2.1.

The quadrupole moment can be related to the nuclear charge deformation:

$$Q_0 = \frac{3}{\sqrt{5\pi}} Z R^2 \beta_2\left(1 + 0.36\beta_2\right) \tag{2.9}$$

with $R = R_0 A^{1/3}$ from the nuclear mass distribution. The deformation is determined by the parameter β_2. β_2 is defined by an angular dependence of the length of the radius vector to the nuclear surface expressed in spherical harmonics [21]. Under the assumption that the valence nucleon is strongly coupled to the core, meaning that the nuclear spin alines with the deformation axis and the quadrupole moment reflects a collective nuclear property, oblate nuclei have a negative quadrupole moment, while prolate nuclei have a positive quadrupole moment. In nuclei prolate deformation is generally favored [28].

The measured quadrupole moment is however not the intrinsic quadrupole moment, but both can be related to one another in the strong-coupling limit:

$$Q_s = \frac{3K^2 - I\left(I+1\right)}{\left(I+1\right)\left(2I+3\right)} Q_0$$

with K the projection of the nuclear spin on the deformation axis.

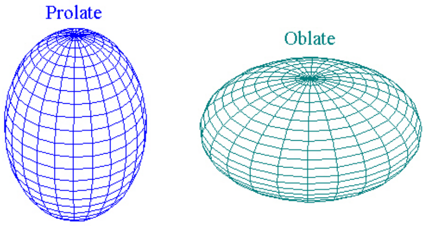

Figure 2.1: The possible axially symmetric deformations from a spherical nucleus.

2.5 Hyperfine parameters

It is possible to determine these nuclear observables from their interaction with the electron cloud of the atom and the resulting perturbations of the atomic energy levels. Each observable gives rise to a different effect in the atomic energy levels: the isotope shift affects the transition centroid; the magnetic dipole moment results in a splitting of the atomic energy levels; the electronic transition probabilities are directly influenced by the nuclear spin; the electric quadrupole moment perturbs those hyperfine levels further. The hyperfine splitting for an atomic transition in ^{202}Fr, having nuclear spin 3 [19], is shown in figure 2.2.

The magnetic dipole hyperfine parameter A is determined by the strength of the interaction between the nuclear dipole moment and the magnetic field produced by the atomic cloud at the position of the nucleus. This interaction lifts the degeneracy of the F-states and causes an energy difference between the atomic fine structure levels (characterised by L, J) and the atomic hyperfine structure levels (characterised by $\vec{F} = \vec{I} + \vec{J}$), given by:

$$\Delta E_F^M = -\frac{A}{2}C$$

with

$$C = F(F+1) - I(I+1) - J(J+1),$$

where F is the hyperfine quantum number that takes values: $|I - J| \leq F \leq I + J$, and A the hyperfine coupling constant

$$A = \frac{\mu_I B_J}{IJ},$$

with B_J the magnetic field induced by the electrons at the site of the nucleus, μ_I the magnetic moment of the nucleus, I the spin of the nucleus and J the total angular momentum of the atomic energy level. Note that there cannot be a magnetic hyperfine splitting for I=0.

The quadrupole moment hyperfine parameter is determined by the interaction of the quadrupole moment of the nucleus with the electric field gradient induced by the electrons at the site of the nucleus. The splitting of the hyperfine levels (F) due to this interaction is given by:

$$\Delta_F^Q = B\frac{\frac{3}{4}C\left(C+1\right)-I\left(I+1\right)J\left(J+1\right)}{2I\left(2I-1\right)J\left(2J-1\right)}, \tag{2.10}$$

where $B = V_{zz}eQ$. Note that the quadrupole hyperfine contribution can only be considered for I>1/2.

In general, it is not possible to calculate B_J and V_{zz} with sufficient precision and relative measurements are performed with respect to a reference isotope. Comparing the values of the A and B parameters to those for a reference isotope, it is then possible to determine the moments of the new isotope relative to those of the reference:

$$\mu = \frac{AI}{A_{ref}I_{ref}}\mu_{ref} \tag{2.11}$$

$$Q = \frac{B}{B_{ref}}Q_{ref} \tag{2.12}$$

Although the extraction of the nuclear observables in hyperfine structure studies is model independent, it strongly depends on the accuracy of the reference values and the measurement of the nuclear spin. The latter is not always guaranteed and can contribute to systematic effects in the interpretation of the results.

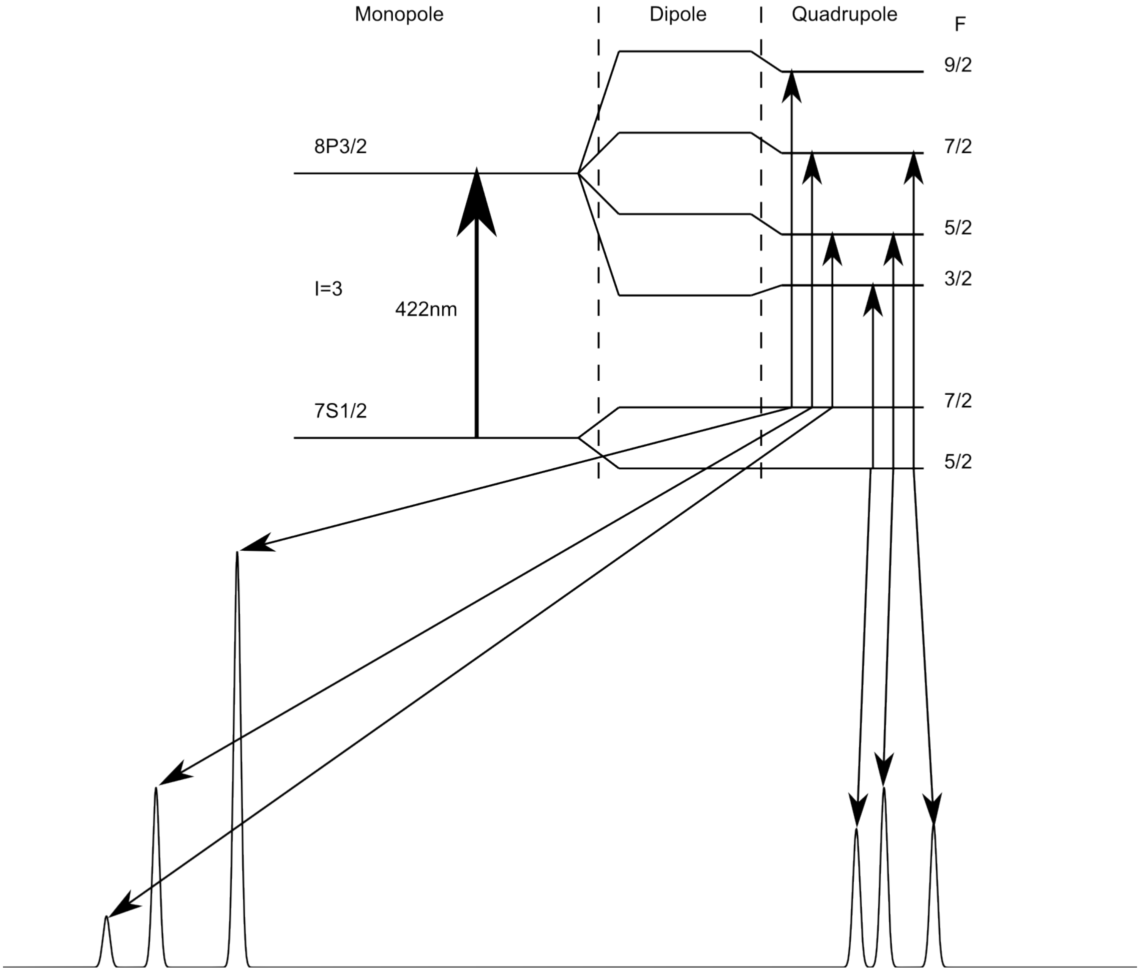

Figure 2.2: A simulated hyperfine spectrum of the experiment on Fr isotopes. The atomic levels used in the experiment are shifted due to the interaction of the atomic electrons with the monopole, dipole and quadrupole moment of the nucleus. The parameters are explained in the text.

Chapter 3

Experimental approach

There are many experimental techniques to determine the nuclear moments. In this work collinear resonance ionization spectroscopy (CRIS) is used. This technique is developed at a new beam line at the ISOLDE facility, CERN. It is an adaption of the more commonly used collinear laser spectroscopy method.

3.1 Collinear laser spectroscopy with optical detection

The concept of laser spectroscopy can be summarized as follows: probing the atom with laser radiation, and extracting model-independent nuclear observables [21]. A schematic diagram of a collinear laser spectroscopy beam line is shown in figure 3.1.

The atoms enter the beam line as ions and are accelerated before neutralization to atoms in a charge-exchange cell. The charge-exchange cell is a chamber filled with an alkali vapor, which due to its chemistry favorably gives away electrons to the incoming ions. A laser beam is overlapped with the atomic beam and if the energy of the photons matches the difference in energy between two atomic levels an electron is excited to a higher level. After the interaction region there is a detection region where the de-excitation photons are detected by photomultiplier tubes.

Due to the collinear geometry, the photons are Doppler shifted relative to the ions. The energy of the photons can be varied using acceleration or deceleration of the ion beam before neutralization. This is easier than scanning the laser frequency itself. By changing the acceleration voltage, the photons are Doppler tuned into resonance. For a co-propagating beam this Doppler shift is:

$$\nu = \nu_L \frac{1-\beta}{\sqrt{1-\beta^2}}, \text{ with } \beta = \sqrt{1 - \frac{m^2c^4}{(eU+mc^2)^2}} \approx \sqrt{\frac{2eU}{mc^2}} \qquad (3.1)$$

where ν_L is the laser frequency, U the potential and m the mass of the ion. Without the Doppler tuning the laser frequency has to be varied, which is technically more challenging. Varying the frequency may also result in a varying power. This will effect the efficiency for the excitation process, challenging the interpretation of the data.

The ions come out of the production target and ion source with an energy spread caused by the environmental conditions of the target and ion source (e.g. high temperature). This energy spread remains constant under acceleration of the ion beam. However, due to conservation of energy, accelerating will reduce the spread in velocity and thus the associated Doppler width of the beam will be reduced.

$$\delta E = \delta\left(\frac{1}{2}mv^2\right) = mv\delta v = \text{constant}$$

The Doppler width obtained for ions accelerated over a voltage U is

$$\delta v_D = v_0 \frac{\delta E}{\sqrt{2eUmc^2}}. \tag{3.2}$$

Inserting realistic numbers yield a Doppler width of about 10MHz for a beam-energy spread of 1eV. This broadening is close to the natural line width of atomic transitions. In practice the experimental resolution is therefore mostly dominated by the laser line width.

The resonantly excited atoms will decay to their ground state by isotropic emission of a photon. These photons are collected by photomultiplier tubes.

There are however limitations to this technique. Optical detection is not very efficient due to a combination of effects. First of all, the collinear geometry is not best suited to offer a large solid angle coverage for optical detection. Combining optical excitation with optical detection induces background: the laser light is scattered by the material inside the beam line and collected by the photomultiplier tubes. Therefore an intense ion beam is necessary, which is a problem for very exotic nuclei. To perform collinear laser spectroscopy yields of 10^4 ions/s are typically necessary [29]. At ISOLDE two isotopes of interest for this work, ^{204,202}Fr, have respectively tabulated yields of 2600 ions/μC and 200 ions/μC [30]. The difference in yield is caused only by the difference in cross section, since lifetimes of both are comparable.

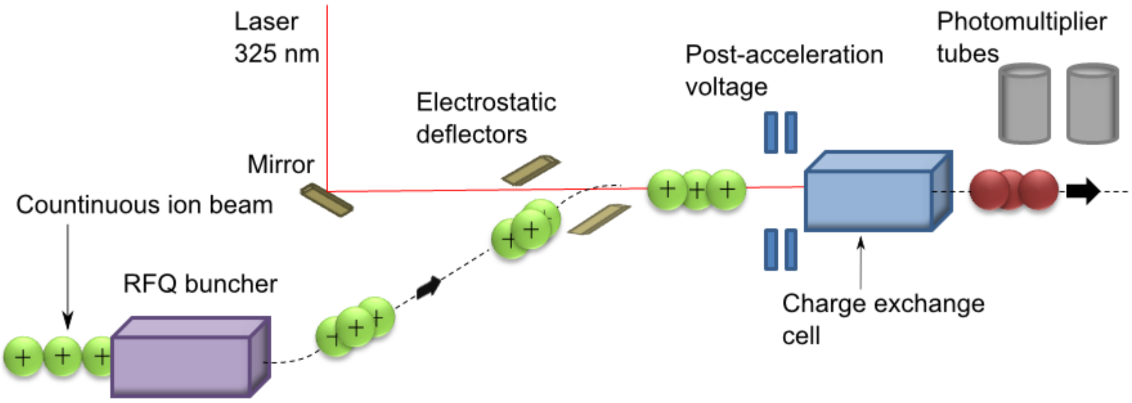

Figure 3.1: A schematic representation of a collinear laser spectroscopy beamline.

3.2 In-source laser spectroscopy

In-source laser spectroscopy makes use of the multiple-step resonant laser excitation-ionization process. In the simplest case, the atoms are first excited with one laser and afterwards ionized with another laser. Only if the first laser frequency is in resonance with the atomic transition, will the second laser be able to ionize the atoms as shown in an example for francium in figure 3.2. Increasing the number of resonant steps before the ionization increases the selectivity of the process [31].

After resonant ionization, the ions can be extracted from the source and counted individually with higher efficiency than detection of photons. It is possible to achieve almost 100% efficiency in ion detection. The technique has a high efficiency, but suffers from a lower resolution. This is mainly caused by target and ion source environment. If the ion source is at a high temperature of about 2500 K, this causes thermal broadening of the line width (of the order of a few GHz), since all atoms in the cavity have high thermal motion. The cross section for the full ionization process is generally somewhat lower than for a single resonant excitation. A higher photon density is therefore required. This is nowadays achieved with pulsed lasers, whose resolution is limited with respect to those used in collinear laser spectroscopy. This way the measurement of the hyperfine structure and especially the splitting due to the quadrupole moment is often compromised. This method is only suited for elements with a large atomic response to the nuclear effect, thus with a large hyperfine splitting of the order of several GHz (Cu, Ag, Au and many heavy elements) [32, 33, 34].

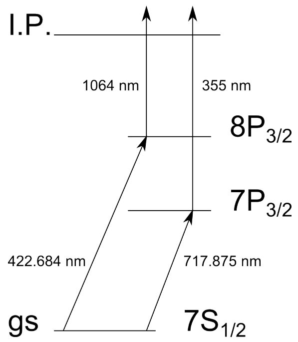

Figure 3.2: Possible ionization schemes for Fr.

3.3 Collinear Resonance Ionization Spectroscopy

Collinear Resonance Ionization Spectroscopy (CRIS) combines the strengths of both techniques. It has the high detection efficiency of ion detection, with the high resolution of collinear laser spectroscopy. A schematic representation of the CRIS beam line at ISOLDE is shown in figure 3.3 and will be described in detail in the following paragraphs.

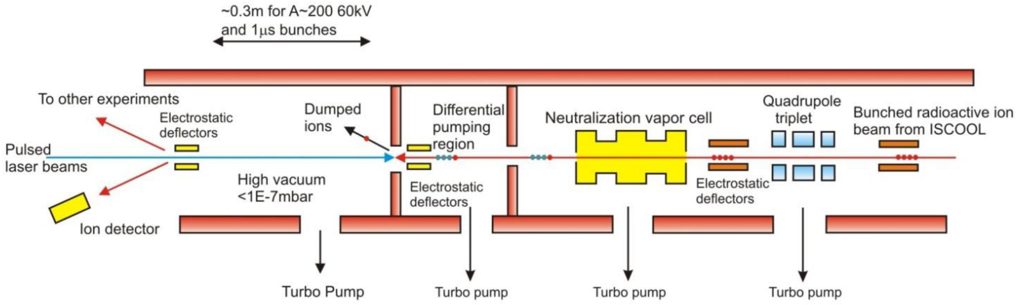

Figure 3.3: A schematic representation of the CRIS beamline at ISOLDE.

3.3.1 Production and delivery

The ISOLDE facility produces isotopes using a 1.4 GeV proton beam impinged upon a thick target. For the purpose of this work the target was a thick UC_x target. UC_x is the target material mostly used at ISOLDE. Because of the thickness of the target the proton energy diminishes and there can be a large variation in isotopes produced by the different reaction mechanisms. The production of isotopes is governed by three major reactions: spallation, fission and fragmentation. Francium is mainly produced by spallation [35]. This is a process where protons, neutrons and alpha particles are ablated from the target nucleus. This way very neutron deficient nuclei can be produced.

After production the atoms diffuse out of the heated target (2300 K) depending strongly on the chemical properties of the reaction products and the target material. The atoms are ionized for extraction towards the separators by a hot tungsten cavity (2300 K). Due to the low ionization threshold of francium the ionization process is almost saturated by this hot cavity system. For this reason it is impossible to study francium by in-source laser spectroscopy. The ions are extracted by a potential difference in the range of 20 to 60kV between the ion source and an extraction electrode [36].

At ISOLDE there are two mass separators: the General Purpose Separator (GPS) and the High Resolution Separator (HRS). These separate the ion beam according to the mass by using a dipole magnet. The quality of the separation is expressed using the mass resolving power. This is the ratio of the mass of the wanted isotope and the full-width-at-half-maximum of the mass separated beam, $\frac{m}{\Delta m}$.

The HRS uses two sets of magnets to increase the sensitivity. This way a mass resolving power of 10600 can be obtained. The easier to operate and more flexible GPS with only one set of magnets can reach 2400 [37]. The CRIS setup uses the ISolde COOLer (ISCOOL) Radio Frequency Quadrupole Cooler-Buncher (RFQCB) which can only be operated with ions coming from HRS due to spatial limitations at ISOLDE.

An RFQCB is an ion guide that uses an RF electric field to confine the ion around the longitudinal axes, a buffer gas to cool the ions and an electrostatic axial field to confine the ions in the axial direction [38]. This way the ions are confined to a three-dimensional space from which they can be released in a bunch. Typically a bunch is released with an energy between 30-60 keV and has a width of 1-5 μs and repitition rate of 10-200 Hz [39, 40].

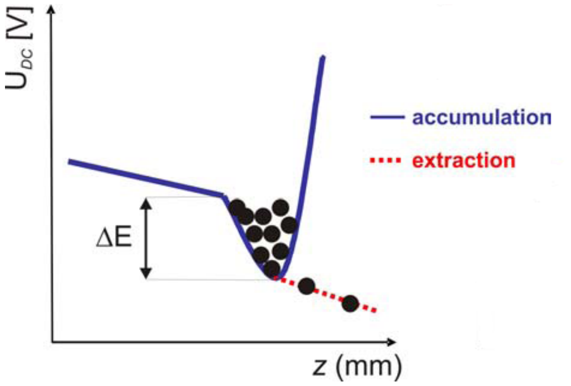

Figure 3.4: A schematic of the bunch extraction of ISCOOL [38].

3.3.2 Charge-exchange cell

After the ion bunch is released from ISCOOL, it is directed to the CRIS beam line, where it passes through the charge-exchange cell (CEC). The CEC neutralizes the ions back to atoms. A block of alkali metal is heated to produce an alkali vapor. This vapor fills a cavity through which the ions pass. The alkali atoms hand off an electron to reach the octet structure and francium is neutralised. For this work potassium was used. In a previous experiment the neutralization efficiency ranged from 50 to 70 %.

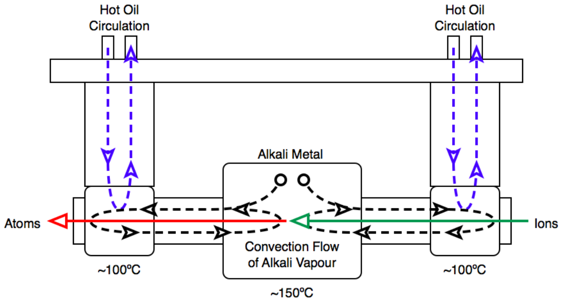

Figure 3.5: A schematic of the CEC [41].

3.3.3 Resonant ionization

After neutralization the atomic bunch enters the interaction region. The interaction region is kept under ultra-high vacuum at a pressure of less than 5×10^{-9} mbar to avoid collisional ionization, which is mainly a problem for elements with a low ionization potential like francium. The atomic beam is overlapped with multiple lasers to resonantly excite an electron beyond the ionization threshold. Adding steps to the process increases selectivity, but may decrease the efficiency (and thus the sensitivity). For francium a two-step ionization scheme was chosen. First a blue 422 nm laser resonantly excites an electron from the $7S_{1/2}$ to the $8P_{3/2}$. Next a high power infrared 1064 nm excites the electron to the continuum and the atom becomes an ion once again. This scheme has the advantage that two-photon ionization with either 1064 nm or 422 nm has a very low cross-section. Therefore the power of both lasers can be increased sufficiently to increase efficiency without enhancing non-resonant ionization. The only limitation is the laser linewidth and power broadening. In this experiment pulsed lasers were used, which typically have a laser linewidth of some GHz, and therefore the resolution is lost to distinguish the different hyperfine transitions within an excited state (in this care the $8P_{3/2}$ state, see fig. 3.6). Therefore, in the future lasers with a much smaller linewidth will be developed for CRIS.

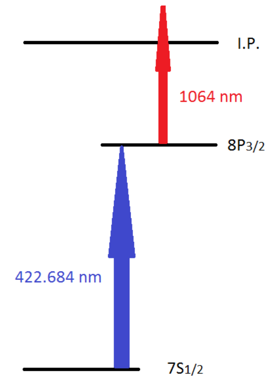

Figure 3.6: The resonant ionization scheme used in this work for Fr.

3.3.4 Detection

The resonant ions are deflected towards a microchannel plate (MCP) as shown in figure 3.7 while neutral atoms are unaffected by the deflection electrode. Thus a very pure beam of selectively resonantly ionized Fr ions is sent to the detection station. The MCP is built from leaded glass with an array of electron multipliers with a diameter of 10-100 μm [42]. A copper plate is mounted before the MCP. The incoming ions strike the surface of the copper plate and secondary electrons are emitted towards the MCP. Like in a photo-multiplier tube a cascade of electrons follows and the electrical signal is amplified. One of the advantages of using an MCP this way is that it is less sensitive to radioactive daughter nuclei being implanted by the ion beam and this way it reduces the background.

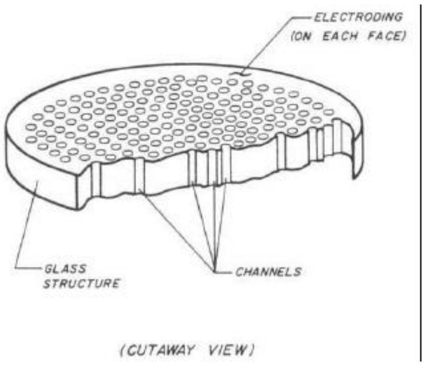

Figure 3.7: A microchannel plate [42].

3.4 Selectivity

CRIS offers the possibility to deliver isomeric pure beams. The beam from the target is mass separated. Isomers have very similar masses as the ground state, so the incoming beam is a mixture of all. The difference in nuclear structure will cause the hyperfine spectrum to be different for ground state and isomer. If one tunes the laser frequency to one of the resonances in the HFS spectrum as shown in figure 3.8, only that isomeric state is excited and remains in the beam. The selectivity of this process is determined by the difference in frequency between the two HFS states, Δ_{AB} and the width of the transition, Γ, by equation

$$S = \left(\frac{\Delta\omega_{AB}}{\Gamma}\right)^2 . \tag{3.3}$$

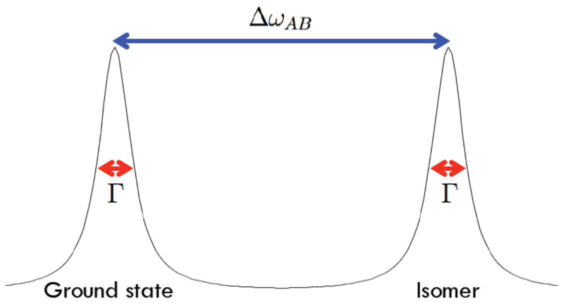

Figure 3.8: The selectivity of exciting an isomer is determined by $\Delta\omega_{AB}$ and Γ.

Increasing the number of excitation steps to ionization increases the selectivity like $S_{total} = S_1 \times S_2 \times S_3 \times \cdots \times S_n$. The trade-off that has to be made is that the efficiency is reduced in every step. Depending on the case choices between sensitivity and selectivity have to be made.

3.5 Decay-Assisted Laser Spectroscopy

Some nuclear isomers may bypass their respective ground state while decaying. Such decay patterns are then identifiable independent from that of the ground state. Therefore, not only its different HFS spectrum, but also its decay is a signature for an isomer. The CRIS beam line has the possibility to selectively ionize an isomeric beam in a particular hyperfine transition and deliver it to a decay spectroscopy station where the radioactive decay is studied [43]. The decay properties allow tagging of peaks in the hyperfine spectrum to the ground state or different isomers. This is the principle of Decay-Assisted Laser Spectroscopy (DALaS).

figure 3.9 shows a HFS spectrum of ^{204}Fr. At least 5 transitions are visible and it was shown that CRIS cannot distinguish the upper level splittings with its current laser linewidth. Therefore, there are at least 3 different nuclear states of ^{204}Fr present. This is as expected [19]. This is where the decay spectroscopy station comes in. Figure 3.10 shows a 20 minute alpha spectrum for each of the first three peaks. It is clear from this decay data that the three peaks correspond to three different states. The case of ^{204}Fr will be discussed in more detail later in the chapter concerning analysis.

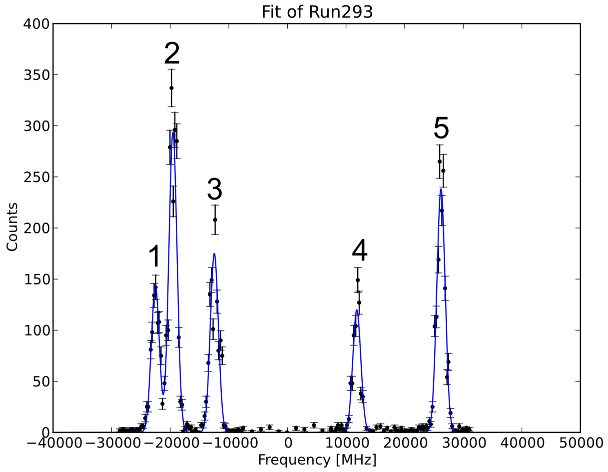

Figure 3.9: A hyperfine spectrum of 204Fr as measured by CRIS.

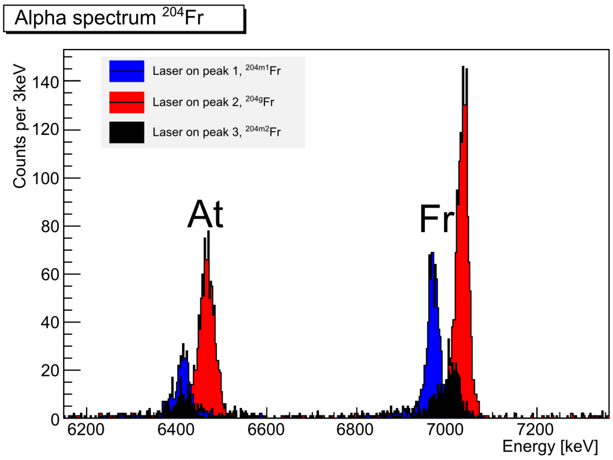

Figure 3.10: The alpha-decay of the ground state and the isomers, observed in the Decay Spectroscopy Station at CRIS, after they were selectively ionized in one of the hyperfine peaks in the spectrum shown in figure 3.9.

Chapter 4

Data collection and analysis

4.1 Technical information

The Doppler tuning electrodes are inside the charge-exchange cell. The alignment of the beamline with the charge-exchange cell is technically challenging. When applying voltage to the electrodes the ion beam was deflected from the beampath. Therefore, instead of Doppler tuning with a voltage, the laser frequency itself was varied. This is in principle more difficult than scanning voltage, but the RILIS collaboration supplied CRIS with a tunable Ti:Sa laser which allowed for scanning laser frequency. An overview of the laser system is given in figure 4.1. The timing sequence that was used to overlap the laser pulses with the incoming ion beam is shown in figure 4.2.

Although the Ti:Sa laser allowed scanning of laser frequency it was not ideally suited for high resolution and high precision measurements. The main issues are the large linewidth and the varying power output. The linewidth makes it impossible to determine the hyperfine splitting of the upper electronic state due to the magnetic dipole moment and the quadrupole moment of the nucleus. The fluctuating power makes it difficult/impossible to rely on the intensities of the peaks for spin determination (the intensity ratio of the different peaks in a spectrum can in general be used to determine the spin of the nucleus [44]). The power fluctuations together with the linewidth makes it impossible to determine the spin of a nucleus with the current data.

The temperature read-out on the charge-exchange cell was not available, therefore the settings from the previous test run in August were used. At that time, the neutralization efficiency was ~40%. This conservative approach was followed for the beginning of the experiment. On the last day of the experiment the current was increased stepwise and a big increase in signal was achieved. The efficiency increased from 1:130 to about 1:60. This gives confidence that in the future CRIS can run with more exotic beams than ^{202}Fr, i.e. be sensitive to lower yields.

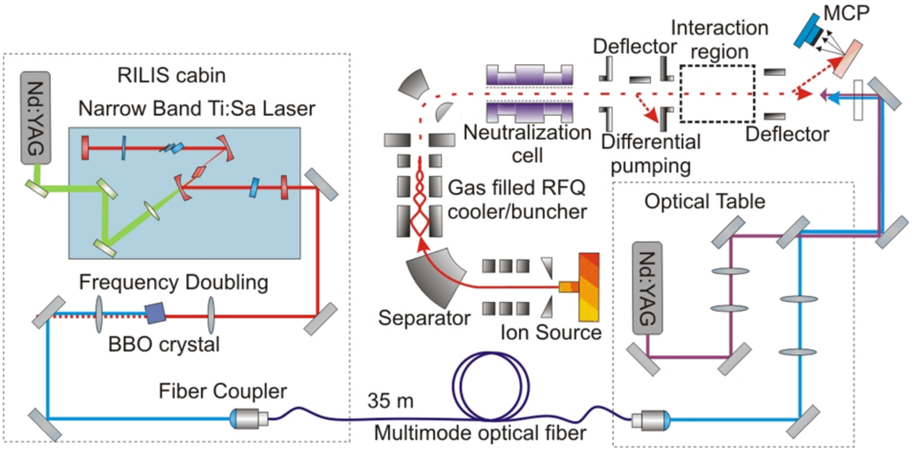

Figure 4.1: A schematic representation of the laser setup used during the experiment.

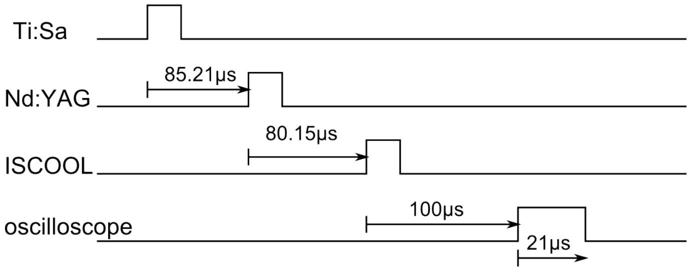

Figure 4.2: The trigger sequence used in the experiment on Fr. The main trigger was the Ti:Sa laser provided by the RILIS collaboration.

4.2 MCP data

The MCP data are recorded using a LeCroy WavePro oscilloscope. This (triggerless digitizer) records the number of ions hitting the MCP in synchronization with each delivered atom bunch. The oscilloscope was connected to a PC via a LabView program. This LabView program constructed a datafile where on every trigger of the Ti:Sa laser the following data was written to the file: time, data, Ti:Sa laser wavenumber, Ti:Sa laser linewidth, Ti:Sa laser power, Nd:YAG laser power, pressure in interaction region, information on the proton (super)cycle and the number of ion counts recorded up to that trigger. At every frequency step a signal was sent to the oscilloscope to clear the number of counts.

4.3 DSS data

At the DSS all data have been recorded on an event-by-event basis by a digital data acquisition system (DGF-4C from XIA). Every detection of a signal in either silicon detectors or in one of the germanium detectors was recorded with a time stamp and energy. This allows to reconstruct possible coincidences offline.

4.4 Analysis procedure

The analysis program used for the HFS data was a code written in Python which takes as input the hyperfine parameters (centroid, A-parameter for the lower atomic level, A-parameter for the upper atomic level and the B-parameter for the upper atomic level), a lineshape and a background which was assumed to be constant. The lineshape was found to be Gaussian and its width is determined by the laser system.

The program builds a spectrum based on the input parameters and this is overlapped with the measured spectrum. The lmfit package used is a shell around the SciPy least-squares fitting routine. It uses the standard Levenberg-Marquardt algorithm. The data points are weighted by their errors. The program returns the resulting best parameters to match the spectrum to the data. A typical fitted spectrum is shown in figure 4.3a

The correlation between the splitting of the lower electronic level and the position of the center frequency is shown in figure 4.3b by a contour map where the chi-square is plotted as a function of both parameters. If there is no correlation between the two parameters, the chi square map will show a pattern around the minimum, elongated along both axes.

The decay data were analyzed using a modified version of the MARABOU code adapted for ROOT to be used with the ISOLDE digital acquisition system. The number of counts are extracted from the decay spectra and analyzed as discussed for the MCP data.

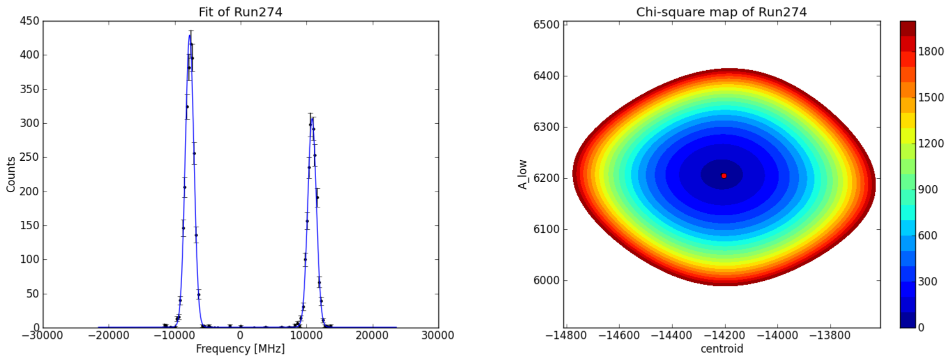

(a) A typical spectrum with a fit by the program used.

(b) A chi-square map of a typical spectrum.

Figure 4.3: The graphical output of the routine used to fit the hyperfine data.

Chapter 5

Analysis and results

The CRIS beam line at ISOLDE just finished its commissioning phase. The data from October 2012 are the first scientific results since the experiment was proposed in 2008.

5.1 Influence of fitting parameters

During the run multiple HFS spectra were obtained of ^{221}Fr for which its hyperfine parameters and nuclear spin are well known [45, 46]. These can be used to determine the influence of different parameters on the data extraction. The parameters of the fitting routine described in chapter 5 are all left as free variables. The relative intensities of the peaks within a multiplet were fixed by angular momentum coupling rules [44], but the intensities of both multiplets were left as free parameters.

5.1.1 Bandwidth of the laser

The lineshape was determined to be Gaussian. The bandwidth of the laser determines the width of the resonance on the spectrum. All six peaks were assumed to have the same linewidth. The results for all spectra of ^{221}Fr are shown in figure 5.1. The average value is 917(44)MHz. This value was used to fix the linewidth in all further analysis of the data.

5.1.2 A-parameters

The A-parameter of ^{221}Fr was measured both for the $7S_{1/2}$ and the $8P_{3/2}$ orbital [46]. Since the spectra do not reveal the hyperfine splitting for the $8P_{3/2}$ orbital the choice can be made to fix its value at zero or fix the ratio between both A-parameters. The results for both approaches are shown in figures 5.2a and 5.2b. From these figures it is clear that fixing the ratio of is the better choice. The hyperfine anomaly can affect the ratio of both A-parameters [47]. For comparison the values from Duong et al [46] are given in table 5.1. The statistical error on the values obtained from

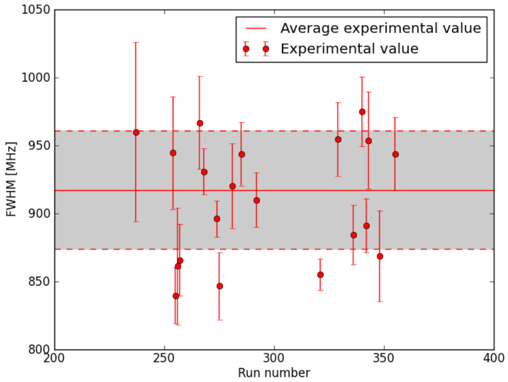

Figure 5.1: The full-width-at-half-maximum of all spectra of ^{221}Fr.

the current experiment is however much larger as can be seen in figure 5.2b. This means that the hyperfine anomaly can be safely ignored. In all further analysis the ratio of ^{221}Fr is used, $\frac{A_{7S_{1/2}}}{A_{8P_{3/2}}} = 277.2$ [46].

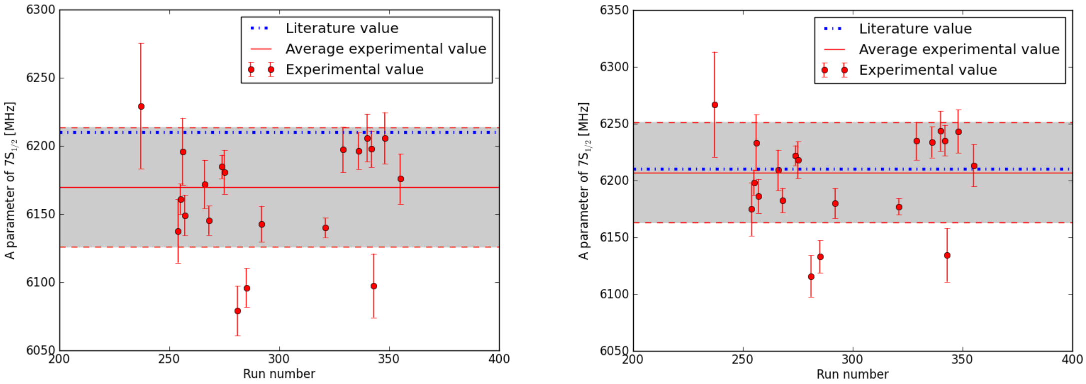

(a) $A_{8P3/2}$ fixed to zero. (b) A fixed ratio between both A-parameters.

Figure 5.2: The value of the A-parameter for the 7S$_{1/2}$ orbital compared to its literature value by Duong et al [46] with the A-parameter of the 8P$_{3/2}$ orbital for two possible values of $A_{8P_{3/2}}$.

	$A_{7S1/2}$	$A_{8P3/2}$	Ratio
^{212}Fr	9064.4(1.5)	32.8(1)	0.003619
^{213}Fr	8757.4(1.9)	31.6(1)	0.003608
^{220}Fr	-6549.2(1.2)	-23.3(1)	0.003558
^{221}Fr	6209.9(1.0)	22.4(1)	0.003607

Table 5.1: The A-parameters for the 7S$_{1/2}$ and the 8P$_{3/2}$ orbital and their ratios [46].

5.1.3 B-parameter

The splitting of the $8P_{3/2}$ orbital due to the quadrupole interaction with the nucleus is too small to be resolved. Therefore the data is not sensitive to the B-parameter. Two possibilities are open to assign values to the B-parameter. Either B is left free as an extra parameter or B is fixed to zero. As shown in figure 5.3, if B is left free it will converge to a value close to the literature value. The statistical spread on the value is 3 orders of magnitude larger than the actual value. Therefore it was chosen to fix B to zero in all further analysis.

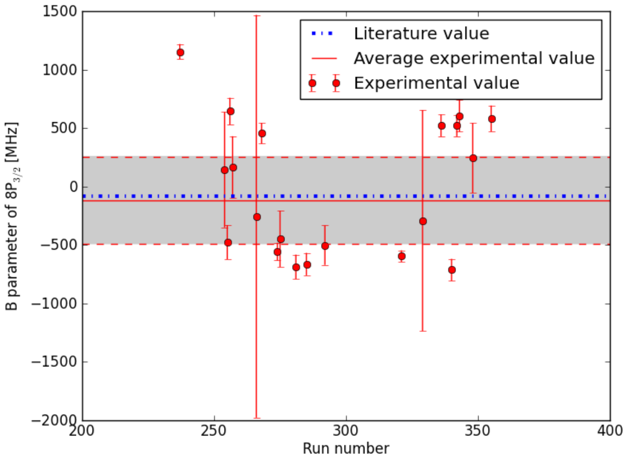

Figure 5.3: The B-parameter value when B is left free to vary.

5.1.4 Intensity ratio

As previously mentioned, it is impossible to use the intensity ratios as proof for a spin assignment. The variation in laser power requires that for the fit we have to use different intensity for the left and the right multiplets. It is however not immediately clear which ratios should be used for the unresolved peaks within each multiplet. One option is to use the angular momentum coupling rules [44], a second option is to assume all the peaks within a multiplet have the same intensity. Both possibilities are shown in figures 5.4a and 5.4b. This shows clearly that using the ratios given by angular momentum coupling is the better option, as could be expected, although both options are within error.

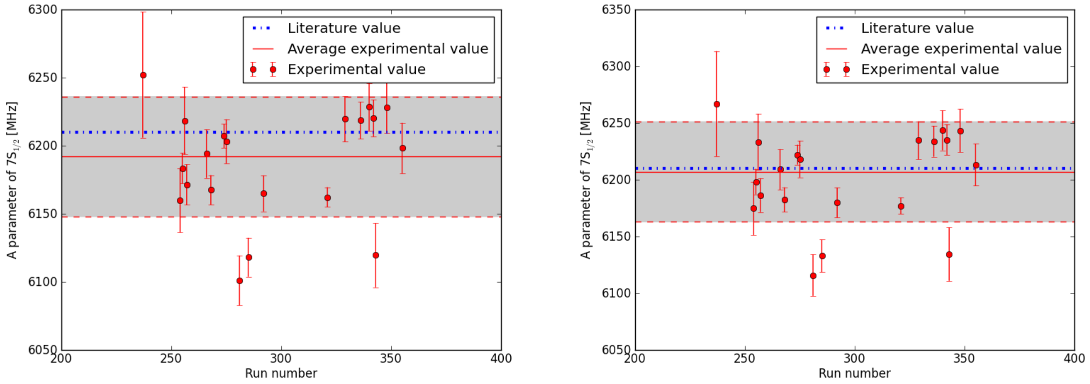

(a) Intensity ratios fixed to an equal value within a multiplet.

(b) Intensity ratios given by angular momentum coupling for peaks within a multiplet.

Figure 5.4: The A-parameter of the $7S_{1/2}$ state as a result of the possible peak-to-peak intensity ratio's.

5.1.5 Reference isotopes

During the experiment multiple reference isotopes were measured to have enough data to compare the transition used by Coc et al [45], $7S_{1/2}$ to $7P_{3/2}$, to the transition used by Duong et al [46], $7S_{1/2}$ to $8P_{3/2}$. The reference isotopes are ^{207}Fr, ^{211}Fr, ^{220}Fr and ^{221}Fr. The results are shown in table 5.2. The isotope shifts are difficult to compare to literature values. Coc et al measured the same isotopes but used a different transition. Although the isotope shift is determined mostly by the $S_{1/2}$ orbital since it penetrates the nucleus, some deviation can be expected if a different excited state is probed.

	$A_{S1/2}$ [MHz]		Isotope shift [MHz]		
Isotope	CRIS	Lit [45]	CRIS	Duong [46]	Coc [45]
^{207}Fr	8482(37)	8484(1)	28471(84)		28809(4)
^{211}Fr	8702(55)	8713.9(8)	24097(67)		24471(4)
^{220}Fr	-6499(57)	-6549.4(9)	2677(112)	2734(11)	2763(5)
^{221}Fr	6207(37)	6204.6(8)	0	0	0

Table 5.2: All values of the A-parameter and isotope shift for the reference isotopes measured by CRIS in October 2012. For completeness the values from the different transition used by Coc et al [45] are also given.

5.2 Results

Using the results of previous analysis, it is possible to extract nuclear observables for the new neutron-deficient isotopes. The isomers in ^{202}Fr and ^{204}Fr require first studying the alpha decay.

5.2.1 Alpha decay

The hyperfine spectra of ^{202}Fr and ^{204}Fr show a multitude of states present. A typical spectrum of ^{204}Fr is shown in figure 5.5. The alpha decay is used to determine which peak belongs to which state. For every peak in the spectrum the Ti:Sa laser was fixed at the center frequency and the alpha decay was monitored for 20 minutes of continuous implantation.

^{204}Fr

Huyse et al [19] reported three different alpha transitions for the three states in ^{204}Fr. The ground state (3^+) has an alpha transition at 7031(5) keV, the (7^+) isomer at 6969(5) keV and the (10^-) isomer at 7013(5) keV. In figure 5.6 the alpha spectra are shown for 3 different settings of the laser frequency, respectively on peak 1, 2 and 3 from figure 5.5. Peak 1 gives alpha lines at 6970(32) keV and 6413(37) keV. These are the alpha lines of respectively the (7^+) isomer and its At daughter. Peak 2 gives alpha lines at 7033(31) keV and at 6467(37) keV. These are the alpha lines of respectively the (3^+) ground state and its At daughter. Peak 3 gives alpha lines at 7016(28) keV and 6415(36) keV. These are the alpha lines of the (10^-) isomer and its At daughter. Analysis of Peak 4 shows that this peak is also due to ionization of the (10^-) isomer of ^{204}Fr. The alpha spectrum of peak 5 in figure 5.5 is shown in figure 5.7. The analysis shows that at this wavenumber a mixture of the (3^+) ground state and the (7^+) isomer is ionized. Although both peaks are overlapping in the hyperfine structure, they are resolved in the alpha decay. The spectrum obtained is shown in figure 5.7 and a ratio is extracted of 1.59 nuclei in the ground state for every nucleus in the (7^+) isomeric state. This ratio is used in the analysis of the hyperfine structure. The assignment of what state corresponds with what peak is summarized in figure 5.5.

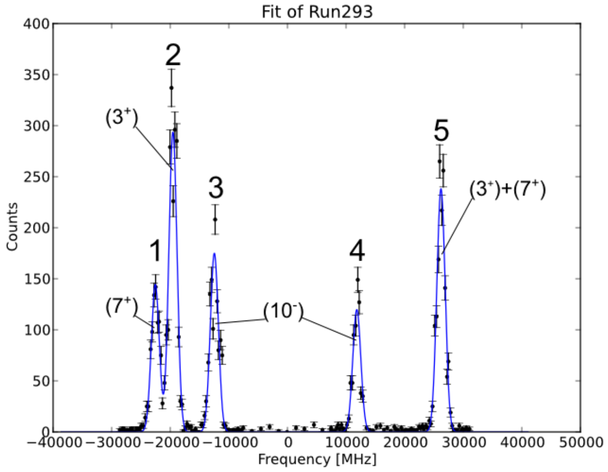

Figure 5.5: A typical hyperfine spectrum of ^{204}Fr obtained by CRIS. Peak 1 corresponds to the (7^+) isomer, peak 2 to the (3^+) ground state and peaks 3 and 4 correspond to the (10^-) isomer, see figure 5.6. Peak 5 is a mixture of the (3^+) ground state and the (7^+) isomer, see figure 5.7.

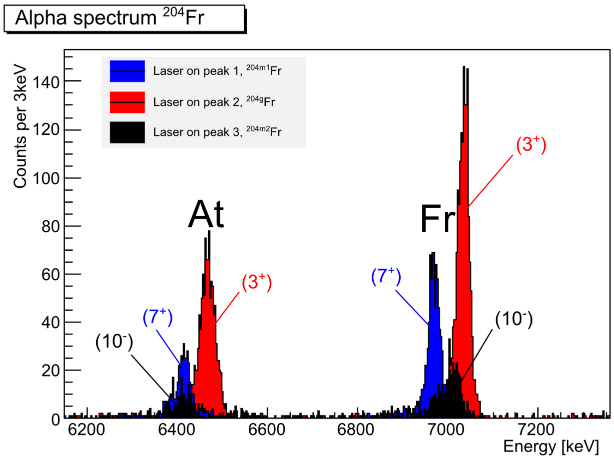

Figure 5.6: The alpha decay of the Fr ground state and isomers and their At daughters as observed using the Decay Spectroscopy Station at CRIS for peaks 1, 2 and 3 in figure 5.5. The alpha spectrum is not shown for peak 4 as this was similar to peak 3. The alpha decay of peak 5 is discussed in figure 5.7.

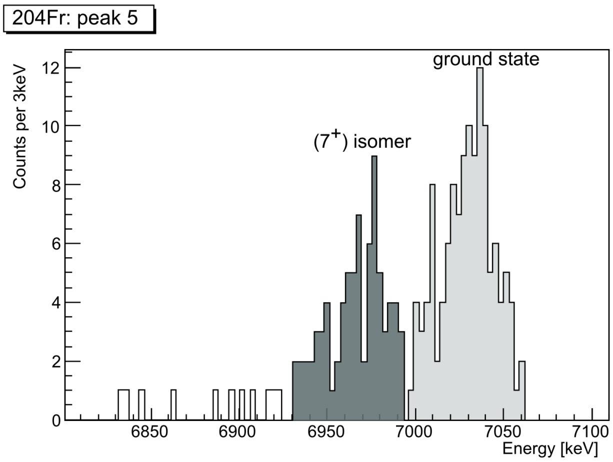

Figure 5.7: The alpha decay of peak 5 in figure 5.5 is a mixture of the (3^+) ground state and (7^+) isomer in ^{204}Fr.

During one of the HFS structure measurements a one minute implantation-collection was performed at each frequency. In the HFS spectrum there is the problem that the resonance of the (7^+) isomer and the (3^+) ground state overlap and in the alpha decay energy spectrum of the (3^+) ground state and the (10^-) isomer overlap, so the combination of alpha decay and hyperfine spectrum is complementary. Figure 5.8 immediately shows that the peaks that are unresolved in either spectrum are resolved in the other. This way it is possible to build a HFS spectrum by gating on the alpha lines. This was however not done for this work due to the low statistics of the one minute implantation-collection.

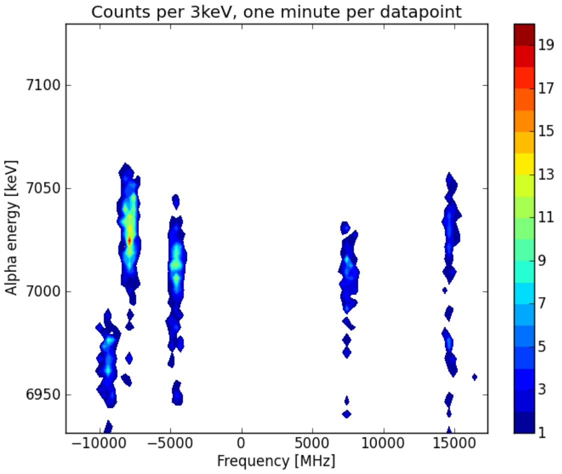

Figure 5.8: Alpha-decay laser-wavenumber matrix. The ability to uniquely identify each hyperfine structure component and each alpha-decay line demonstrates the power of the CRIS technique.

^{202}Fr

The situation is more difficult for ^{202}Fr since both alpha decay transitions have similar energy, 7241(8) keV for the (3^+) ground state and 7235(8) keV for the (10^-) isomeric state [12], and the alpha-peaks are thus unresolved. The daughter states in ^{198}At have alpha decay transitions at respectively 6748(6) keV and 6850(6) keV which can be resolved and therefore they are used to tag the hyperfine spectrum. The HFS spectrum obtained in October 2012 is shown in figure 5.9. Since ^{202}Fr and ^{204}Fr have similar nuclear structure, it is likely that both share similar hyperfine spectra. This is supported by the decay information as shown in figure 5.9. Due to the low statistics of these 20 minute implantation-collection spectra, fitting is impossible. The average values are however consistent with the alpha transitions in ^{198}At. The assignment based on the alpha decay of which peak in the HFS spectrum belongs to which state is presented in figure 5.9.

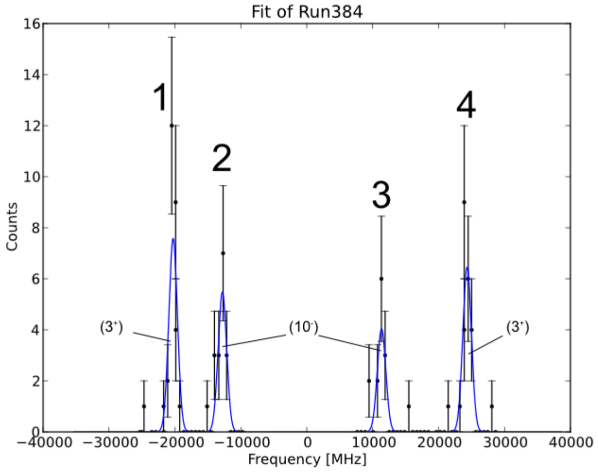

Figure 5.9: A typical hyperfine spectrum of ^{202}Fr obtained by CRIS. The assignment is based on the alpha decay shown in figure 5.10.

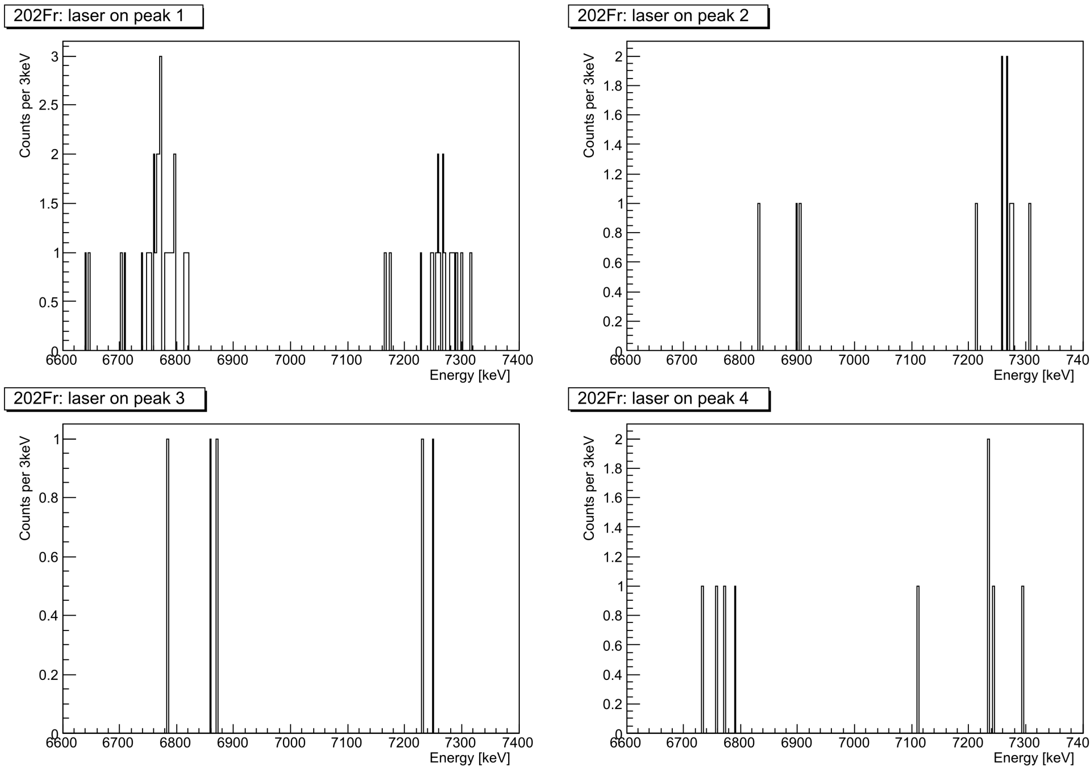

Figure 5.10: A comparison of the alpha spectra for all 4 peaks in the spectrum shown in figure 5.9. Using the transitions in ^{202}Fr it is impossible to distinguish both states. The average value of the decay of the ^{198}At daughters however, allows to distinguish both parent states. Peak 1 and 4 in figure 5.9 belong to the (3^+) ground state and peaks 2 and 3 belong to the (10^-) isomeric state.

^{203,205}Fr

In ^{203}Fr an isomer is expected with a half life of 60 ms and a spin of ($1/2^+$) [13]. This is the deformed proton intruder state mentioned in chapter 2. It was however not observed. In ^{205}Fr again no isomers were observed. Therefore no alpha decay energy spectra were measured.

5.2.2 Hyperfine structure

Over the course of the experiment, three spectra of the hyperfine structure of ^{204}Fr were measured, two of ^{203}Fr, one of ^{202}Fr and one of ^{205}Fr. The results are summarized in table 5.3.

Isotope	Spin	A-parameter (7S1/2) [MHz]	μ [μ_0]	Isotope shift [MHz]	$\delta\langle r^2\rangle$ [fm^2]
202gFr	3	12820(37)	3.92(8)	32682(91)	-1.582(17)
202mFr	10	2314(37)	2.36(5)	32540(106)	-1.575(17)
203Fr	9/2	8189(37)	3.76(8)	31344(103)	-1.517(17)
204gFr	3	13018(37)	3.98(8)	32084(120)	-1.553(17)
204m1Fr	7	6515(37)	4.65(10)	32035(91)	-1.551(17)
204m2Fr	10	2309(37)	2.35(6)	30945(187)	-1.498(18)
205Fr	9/2	8395(37)	3.85(8)	30294(91)	-1.467(16)
207Fr	9/2	8482(37)	3.89(8)	28446(91)	-1.377(15)
211Fr	9/2	8702(55)	3.99(9)	24072(91)	-1.165(13)
220Fr	1	-6499(57)	-0.66(1)	2652(111)	-0.128(6)
221Fr	5/2	6186(37)	1.58(3)	0	0

Table 5.3: The results obtained by CRIS in October 2012 using the $8P_{3/2}$ transition.

5.2.3 Isotope shift and change in mean-square charge radii

The transition from isotope shift to change in mean-square charge-radius can be made according to equation 2.2:

$$\delta\nu_i^{A,A'} = M_i \frac{A' - A}{AA'} + F_i \delta\langle r^2\rangle^{A,A'}, \tag{5.1}$$

with M_i the mass shift factor and F_i the field shift factor. The coefficients of the mass and field shift have been obtained for the $7S_{1/2}$ to $7P_{3/2}$ by Coc et al [45]. Duong et al [46] extended this result to the $7S_{1/2}$ to $8P_{3/2}$ transition using a King plot [25]. Equation 5.1 is valid for all transitions and the variation in charge-radius can be taken out of the equation when comparing two different transition. A linear relationship is obtained and the relative field and mass shift factors can be extracted. For two transitions i and j we get

$$\left(\frac{AA'}{A' - A}\delta\nu_j^{A,A'}\right) = \frac{F_j}{F_i}\left(\frac{AA'}{A' - A}\delta\nu_i^{A,A'}\right) + M_j - \frac{F_j}{F_i}M_i. \tag{5.2}$$

The results by Duong et al are extended by adding the data from CRIS to their data. The values for the field and mass shift of the transition used by Coc et al [45] have been recalculated by Dzuba et al [48], F=-20766(208) MHz/fm^2 and M=650(320) GHz amu for the $7P_{3/2}$ transition. When using this result, values of F=-20656(219) MHz/fm^2 and M=677(396) GHz are obtained for the $8P_{3/2}$. The charge radii are reported in table 5.3 and discussed in the next chapter.

5.3 Magnetic dipole moments

The magnetic moments can be extracted using equation 2.11:

$$\mu = \frac{AI}{A_{ref} I_{ref}} \mu_{ref}.$$

The measurement of ^{207}Fr is taken as the reference, with $\mu_{ref} = 3.89(8)$ and $I_{ref} = 9/2$. For A_{ref} the value of 8482(37) MHz from the experiment was used. The results are summarized in table 5.3 and discussed in the next chapter.

Chapter 6

Discussion

6.1 g-factor and magnetic moment

As mentioned in the chapter on nuclear moments, the g-factor is a signature for the nuclear quantum configurations. The g-factor is obtained from the fitted A-factor, provided the correct spin is used to fit the data. The earlier tentative assigned spins [19] have been used for this data analysis. The g-factor is then obtained by $g = \mu/I$.

6.1.1 Odd-A isotopes

The g-factors of the odd-A francium isotopes below N=126 are given in table 6.2 and shown in figure 6.1. It is clear that the configuration of the ground state wave function remains $\pi h_{9/2}$ also in ^{205}Fr and ^{203}Fr as expected from literature. The $\pi 3s_{1/2}$ orbit is not (yet) the ground state configuration.

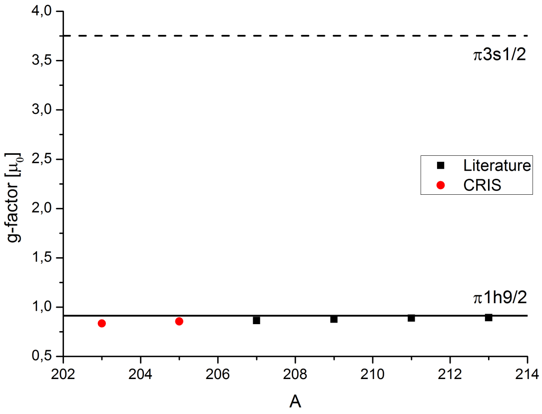

Figure 6.1: The g-factors for the odd-A isotopes of francium below N=126. Data on $^{207-213}$Fr are taken from Ekstrom et al [49]. The line of the $\pi 1h_{9/2}$ g-factor was taken from ^{209}Bi [50] and for the $\pi 3s_{1/2}$ orbit the g-factor of ^{207}Tl [51] was used.

Orbit	isotope	g_{exp}
$\pi 1h_{9/2}$	^{203}Fr (this work)	0.836
$\nu 3p_{3/2}$	^{201g}Po [52]	-0.627
$\nu 2f_{5/2}$	^{205}Rn [49]	0.229
$\nu 1i_{13/2}$	^{201m}Po [52]	-0.153

Table 6.1: The experimental g-factors used to calculate an empirical estimate of the assumed single-particle configurations.

Isotope	Configuration (I^{π})	g_{emp}	g_{exp}
^{202g}Fr	$\left[\pi 1h_{9/2} \otimes \nu 3p_{3/2}\right]_{3+}$	1.45	1.31(3)
^{202m}Fr	$\left[\pi 1h_{9/2} \otimes \nu 1i_{13/2}\right]_{10-}$	0.23	0.24(1)
^{203}Fr	$\left[\pi 1h_{9/2}\right]_{9/2+}$	0.91	0.84(1)
^{204g}Fr	$\left[\pi 1h_{9/2} \otimes \nu 3p_{3/2}\right]_{3+}$	1.45	1.33(3)
^{204m1}Fr	$\left[\pi 1h_{9/2} \otimes \nu 2f_{5/2}\right]_{7+}$	0.69	0.66(1)
^{204m2}Fr	$\left[\pi 1h_{9/2} \otimes \nu 1i_{13/2}\right]_{10-}$	0.23	0.24(1)
^{205}Fr	$\left[\pi 1h_{9/2}\right]_{9/2+}$	0.91	0.86(1)

Table 6.2: The values of the experimental g-factors compared to the empirical calculation for the assigned configurations. The empirical calculation for the even-A isotopes is based on the values from table 6.1.

6.1.2 Even-A isotopes

The g-factors of the even-A francium isotopes are compared to an empirical coupling of an unpaired proton with an unpaired neutron according to equation 2.8. To include effects of configuration mixing, the moments of the neutron and proton orbits are taken from isotopes near the isotopes of interest. For the proton $\mathrm{h}_{9/2}$ orbit the g-factor from ^{203}Fr is used. The neutron g-factors are used from ^{201}Po for the neutron $3\mathrm{p}_{3/2}$, ^{205}Rn for the neutron $2\mathrm{f}_{5/2}$ and ^{201}Po for the neutron $1\mathrm{i}_{13/2}$. The values used are summarized in table 6.1. The g-factors deduced from our experimental magnetic moments are compared to these empirical g-factors for assumed single-particle configurations are in table 6.2 and shown in figure 6.2.

The good agreement between the experimental g-factor of the (10^-) isomers in ^{202}Fr and ^{204}Fr and the empirical g-factor of the $\left[\pi 1h_{9/2} \otimes \nu 1i_{13/2}\right]_{10-}$ configuration provides further proof for the tentative assigment made by Huyse et al [19] independent of this earlier work. There is also good agreement for the experimental g-factor of the (7^+) isomer in ^{204}Fr with the empirical g-factor for the $\left[\pi 1h_{9/2} \otimes \nu 2f_{5/2}\right]_{7+}$ configuration. This is again further proof for the tentative assignment made in the earlier work.

The g-factors of the (3^+) ground states in ^{202}Fr and ^{204}Fr are suggesting a mixed configuration, where the $\left[\pi 1h_{9/2} \otimes \nu 3p_{3/2}\right]_{3+}$ configuration is the dominant config-

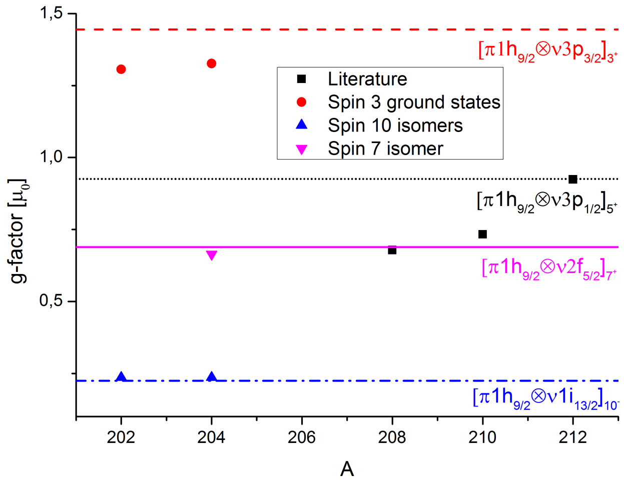

Figure 6.2: The g-factors for the even-A francium isotopes using the proposed spins by Huyse et al [19]. For comparison the empirical moments of the neutron orbits with the proton $1h_{9/2}$ orbit from table 6.2 are shown as a line.

uration. This is contradictory to the results by Huyse et al [19] which assigned the neutron $\left[\pi 1h_{9/2}\otimes\nu 2f_{5/2}\right]_{3+}$ as the leading configuration for the ground states. However, these assignments were based on earlier work by the same group on bismuth by Van Duppen et al [18]. In that work the configuration of the ground state for ^{194}Bi and ^{196}Bi was proposed as either $\left[\pi 1h_{9/2}\otimes\nu 3p_{3/2}\right]$ or $\left[\pi 1h_{9/2}\otimes\nu 2f_{5/2}\right]$. This work confirms that it is the former.

6.2 Change in mean-square charge radii

The change in mean-square charge radii over an isotopic chain is a signature for the nuclear shape. In figure 6.3 the change in charge radii of francium, polonium and lead is shown. Lead remains spherical over the entire chain, while polonium starts to depart from the trend of spherical droplet around N=114. Francium start to deviate already at N=118 (N=119 is not measured). This earlier onset of deformation is reason to believe that the extra protons polarize the nucleus, so that it is more sensitive to deformation.

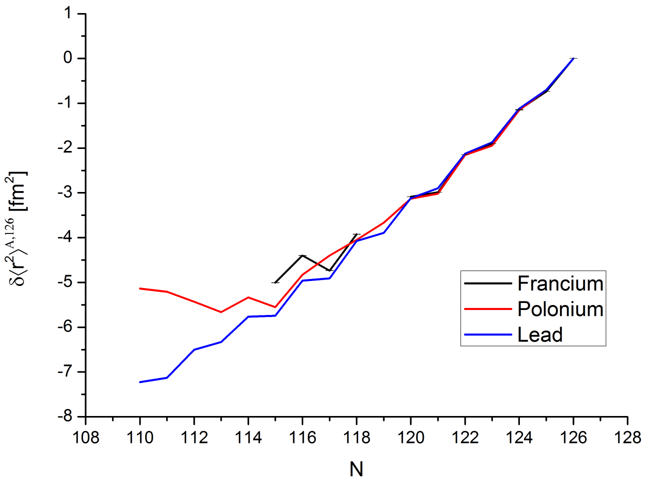

Figure 6.3: The change in charge radii for the ground states of lead [24], polonium [53, 17] and francium [48].

The mean square charge radii for the ground state and isomeric states are shown in figure 6.4. The (3^+) ground state and the (10^-) isomer in ^{204}Fr have completely different charge radii and thus a different shape. This can be seen as a case of shape coexistence. The reason why these charge radii are so different compared to ^{202}Fr is unclear and requires further investigation.

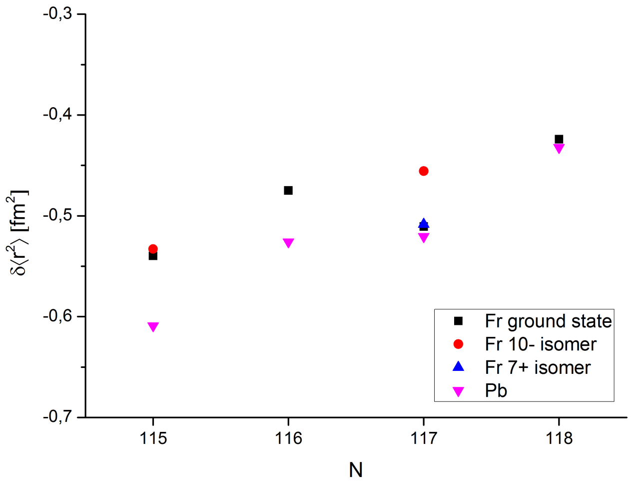

Figure 6.4: The mean square charge radius for the ground states and isomers in $^{202-205}$Fr as determined in this work.

Chapter 7

Conclusion and outlook

Collinear Resonance Ionization Spectroscopy was proven to be a successful new technique. The increased efficiency and the reduction in background have lead to new physics results down to ^{202}Fr (100 ions/s). The Decay Spectroscopy Station allowed for alpha decay tagging of the peaks in the optical hyperfine spectrum. This way we were able to untangle the hyperfine spectra of separate states of the same isotope.

The field shift factor and mass shift factor obtained by Duong et al [46], using the same $8P_{3/2}$ transition as in this work, were improved by including new isotopes from this work which were already measured with the $7P_{3/2}$ transition by Coc et al [45] and taking the new calculated input values from Dzuba et al [48].

The magnetic moments of neutron-deficient francium isotopes below N=120 were determined for the first time. The protons in the ground state in the odd-A isotopes remains in the $\pi h_{9/2}$ single-particle configuration as expected. However, charge radii suggest deformation. No isomers in either ^{203}Fr or ^{205}Fr have been observed. In the even-A francium cases of ^{204}Fr and ^{202}Fr, the work done by Huyse et al [19] and Van Duppen et al [18] has been confirmed and extended. There is strong evidence in the g-factors pointing to the (3^+) ground state being dominated by $\left[\pi 1h_{9/2} \otimes \nu 3p_{3/2}\right]$ with some small admixture from the $\left[\pi 1h_{9/2} \otimes \nu 2f_{5/2}\right]$. The g-factors of the (10^-) isomers allow for a confident assignment of $\left[\pi 1h_{9/2} \otimes \nu 1i_{13/2}\right]$. The g-factor of the (7^+) isomer in ^{204}Fr strongly suggests that this is indeed a coupling of $\left[\pi 1h_{9/2} \otimes \nu 2f_{5/2}\right]$.

The change in mean-square charge radii of neutron deficient isotopes has been determined below N=120. A departure from sphericity is observed at N=116, earlier than in polonium. This could prove that adding protons to the nucleus effectively polarizes the nucleus more strongly. Whether this departure from sphericity is caused by dynamic or static deformation has to be determined by measuring the electric quadrupole moment. The difference in charge-radius between the (3^+) ground state and (10^-) isomer in ^{204}Fr can be considered a case of shape coexistence.

The increased efficiency near the end of the experiment promises a higher count rate for the more exotic cases. Therefore the CRIS beam line is expected to be able to measure the isomer in ^{203}Fr and the ground state and isomer in ^{201}Fr.

A measurement of ^{206}Fr was performed but as no alpha decay data have been collected, it is impossible to determine which peaks in the hyperfine spectra correspond to which of the three states present. A re-measurement of this isotope is planned, with dedicated time proposed for studying the three states with DALaS.

It will be interesting to compare the change in charge radii for different isotope chains in the same region. Recent data on astatine, thallium and gold are under analysis by a different group.

Bibliography

[1] L. Meitner and O. R. Frisch. Disintegration of Uranium by Neutrons: a New Type of Nuclear Reaction. *Nature*, 143:239–240, 1939.

[2] G. Royer and R. Rousseau. On the Coefficients of the Liquid Drop Model Mass Formulae and Nuclear Radii. *The European Physical Journal A*, 807(3-4):19, 2009.

[3] M. G. Mayer. On Closed Shells in Nuclei. *The Physical Review*, 74(3):235–239, 1948.

[4] M. G. Mayer. Nuclear Configurations in the Spin-Orbit Coupling Model. I Empirical Evidence. *Physical Review*, 78(1):16–21, 1950.

[5] K. Heyde. *The Nuclear Shell Model*. Springer-Verlag, 1990.

[6] P. Ring and P. Schuck. *The Nuclear Many-Body Problem*. Springer-Verlag, 1980.

[7] A. Ozawa, T. Kobayashi, T. Suzuki, K. Yoshida, and I. Tanihata. New Magic Number, $\mathrm{N} = 16$, Near the Neutron Drip Line. *Physical review letters*, 84(24):5493–5, 2000.

[8] A. N. Andreyev, M. Huyse, P. Van Duppen, L. Weissman, D. Ackermann, J. Gerl, F. P. Hessberger, S. Hofmann, A. Kleinbohl, G. Munzenberg, S. Reshitko, C. Schlegel, H. Schaffner, P. Cagarda, M. Matos, S. Saro, A. Keenan, C. Moore, C. D. O'Leary, R. D. Page, M. Taylor, H. Kettunen, M. Leino, A. Lavrentiev, R. Wyss, and K. Heyde. A Triplet of Differently Shaped Spin-zero States in the Atomic Nucleus ^{186}Pb. *Nature*, 405:186–189, 2000.

[9] Brookhaven National Laboratory. Evaluated nuclear structure database files.

[10] Z. Kalaninová, A. N. Andreyev, S. Antalic, F. P. Heß berger, D. Ackermann, B. Andel, M. C. Drummond, S. Hofmann, M. Huyse, B. Kindler, J. F. W. Lane, V. Liberati, B. Lommel, R. D. Page, E. Rapisarda, K. Sandhu, Š. Šáro, A. Thornthwaite, and P. Van Duppen. Alpha-Decay of the Very Neutron-Deficient Isotopes $^{197\text{-}199}$Fr. *Physical Review C*, 87(4):044335, 2013.

[11] U. Jakobsson, J. Uusitalo, S. Juutinen, M. Leino, T. Enqvist, P. T. Greenlees, K. Hauschild, P. Jones, R. Julin, S. Ketelhut, P. Kuusiniemi, M. Nyman, P. Peura, P. Rahkila, P. Ruotsalainen, J. Sarén, C. Scholey, and J. Sorri. Recoil-Decay Tagging Study of ^{205}Fr. *Physical Review C*, 85(1):014309, 2012.

[12] J. Uusitalo, M. Leino, T. Enqvist, K. Eskola, T. Grahn, P. Greenlees, P. Jones, R. Julin, S. Juutinen, A. Keenan, H. Kettunen, H. Koivisto, P. Kuusiniemi, A.-P. Leppänen, P. Nieminen, J. Pakarinen, P. Rahkila, and C. Scholey. Alpha Decay Studies of Very Neutron-Deficient Francium and Radium Isotopes. *Physical Review C*, 71(2):024306, 2005.

[13] U. Jakobsson, S. Juutinen, J. Uusitalo, M. Leino, K. Auranen, T. Enqvist, P. T. Greenlees, K. Hauschild, P. Jones, R. Julin, S. Ketelhut, P. Kuusiniemi, M. Nyman, P. Peura, P. Rahkila, P. Ruotsalainen, J. Sarén, C. Scholey, and J. Sorri. Spectroscopy of the Proton Drip-Line Nucleus \superscript{203}Fr. *Physical Review C*, 87(5):054320, 2013.

[14] F. Le Blanc, D. Lunney, J. Obert, J. Oms, J. C. Putaux, B. Roussiere, J. Sauvage, S. Zemlyanoi, J. Pinard, L. Cabaret, H. T. Duong, G. Huber, M. Krieg, V. Sebastian, J. E. Crawford, J. K. P. Lee, M. Girod, S. Peru, and J. Genevey. Large Odd-Even Radius Staggering in the Very Light Platinum Isotopes from Laser Spectroscopy. *Physical Review C*, 60:054310, 1999.

[15] G. Ulm, S. K. Bhattecherjee, P. Dabkiewicz, G. Huber, H.-J. Kluge, T. Kühl, H. Lochmann, E.-W. Otten, K. Wendt, S.A. Ahmad, W. Klempt, R. Neugart, and ISOLDE Collaboration. Isotope Shift of ^{182}Hg and an Update of Nuclear Moments and Charge Radii in the Isotope Range ^{181}Hg-^{206}Hg. *Zeitschrift für Physik A*, 325:247–259, 1986.

[16] I. Angeli and K. P. Marinova. Table of Experimental Nuclear Ground State Charge Radii: An Update. *Atomic Data and Nuclear Data Tables*, 99(1):69–95, 2013.

[17] M. D. Seliverstov, T. E. Cocolios, W. Dexters, A. N. Andreyev, S. Antalic, A. E. Barzakh, B. Bastin, J. Büscher, I. G. Darby, D. V. Fedorov, V. N. Fedoseyev, K. T. Flanagan, S. Franchoo, S. Fritzsche, G. Huber, M. Huyse, M. Keupers, U. Köster, Yu. Kudryavtsev, B. A. Marsh, P. L. Molkanov, R. D. Page, A. M. Sjø din, I. Stefan, J. Van de Walle, P. Van Duppen, M. Venhart, and S. G. Zemlyanoy. Charge Radii of Odd-A $^{191\text{-}211}$Po Isotopes. *Physics Letters B*, 719(4-5):362–366, 2013.

[18] P. Van Duppen, P. Decrock, P.. Dendooven, M. Huyse, G. Reusen, and J. Wauters. Intruder States in Odd-Odd Tl Nuclei Populated in the Alpha-Decay of Odd-Odd Bi Isotopes. *Nuclear Physics A*, 529:268–288, 1991.

[19] M. Huyse, P. Decrock, P. Dendooven, G. Reusen, P. Van Duppen, and J. Wauters. Isomers in Three Doubly Odd Fr-At-Bi Alpha-Decay Chains. *Physical Review C*, 46(4):1209–1217, 1992.

[20] R. Menges, U. Dinger, N. Boos, G. Huber, S. Dutta, R. Kirchner, O. Klepper, T. Kiihl, D. Marx, and G. D. Sprouse. Nuclear Moments and the Change in the Mean Square Charge Radius of Neutron Deficient Thallium Isotopes. *Zeitschrift für Physik A*, 341:475–479, 1992.

[21] R. Neugart and G. Neyens. *The Euroschool Lectures on Physics With Exotic Beams, Vol. II: Nuclear Moments*, volume 189. Springer, 2006.

[22] V. Paar. A Parabolic Rule for the Energy Dependence on x=I(I+1) for Proton-Neutron Multiplets in Odd-Odd Nuclei. *Nuclear Physics A*, 331:16–28, 1979.

[23] B Cheal, E Mané, J Billowes, M L Bissell, K Blaum, B a Brown, F C Charlwood, K T Flanagan, D H Forest, C Geppert, M Honma, A Jokinen, M Kowalska, A Krieger, J Krämer, I D Moore, R Neugart, G Neyens, W Nörtershäuser, M Schug, H H Stroke, P Vingerhoets, D T Yordanov, and M Záková. Nuclear Spins and Moments of Ga Isotopes Reveal Sudden Structural Changes Between N=40 and N=50. *Physical Review Letters*, 104(25):252502, 2010.

[24] M. Wang, G. Audi, A. H. Wapstra, F. G. Kondev, M. MacCormick, X. Xu, and B Pfeiffer. The Ame2012 Atomic Mass Evaluation. *Chinese Physics C*, 36(12):1603–2014, 2012.

[25] W. H. King. Comments on the Article: Peculiarities of the Isotope Shift in the Samarium Spectrum. *Journal fo the Optical Society of America*, 53(5):638–639, 1963.

[26] B. Cheal, T. E. Cocolios, and S. Fritzsche. Laser Spectroscopy of Radioactive Isotopes: Role and Limitations of Accurate Isotope-Shift Calculations. *Physical Review A*, 86(4):042501, 2012.

[27] J. Papuga, M. L. Bissell, K. Kreim, K. Blaum, B. A. Brown, M. De Rydt, R. F. Garcia Ruiz, H. Heylen, M. Kowalska, R. Neugart, G. Neyens, W. Nörtershäuser, T. Otsuka, M. M. Rajabali, R. Sánchez, Y. Utsuno, and D. T. Yordanov. Spins and Magnetic Moments of ^{49}K and ^{51}K: Establishing the $1/2^+$ and $3/2^+$ Level Ordering Beyond N=28. *Physical Review Letters*, 110(17):172503, 2013.

[28] R. F. Casten. *Nuclear Structure From A Simple Perspective.* Oxford University Press, 1990.

[29] P. Vingerhoets, K. T. Flanagan, M. Avgoulea, J. Billowes, M. L. Bissell, K. Blaum, B. A. Brown, B. Cheal, M. De Rydt, D. H. Forest, Ch. Geppert, M. Honma, M. Kowalska, J. Krämer, A. Krieger, E. Mané, R. Neugart,

G. Neyens, W. Nörtershäuser, T. Otsuka, M. Schug, H. H. Stroke, G. Tungate, and D. T. Yordanov. Nuclear Spins, Magnetic Moments, and Quadrupole Moments of Cu Isotopes from N=28 to N=46: Probes for Core Polarization Effects. *Physical Review C*, 82(6):064311, 2010.

[30] S. Lukic, F. Gevaert, A. Kelic, M. V. Ricciardi, K. H. Schmidt, and O. Yordanov. Systematic Comparison of ISOLDE-SC Yields with Calculated In-Target Production Rates. *Nuclear Instruments and Methods in Physics Research Section A: Accelerators, Spectrometers, Detectors and Associated Equipment*, 565(2):46, 2006.

[31] V. N. Fedosseev, Yu. Kudryavtsev, and V. I. Mishin. Resonance Laser Ionization of Atoms for Nuclear Physics. *Physica Scripta*, 85(5):058104, 2012.

[32] T. E. Cocolios, A. N. Andreyev, B. Bastin, N. Bree, J. Büscher, J. Elseviers, J. Gentens, M. Huyse, Yu. Kudryavtsev, D. Pauwels, T. Sonoda, P. Van den Bergh, and P. Van Duppen. Magnetic Dipole Moments of ^{57,58,59}Cu. *Physical Review C*, 81(1):014314, 2010.

[33] F. Le Blanc, J. Obert, J. Oms, J. C. Putaux, B. Roussière, and J. Sauvage. Nuclear Moments and Deformation Change in ^{184}Au^{g,m} from Laser Spectroscopy. *Physical Review Letters*, 79(12):2213–2216, 1997.

[34] L. Weissman, U. Köster, R. Catherall, S. Franchoo, U. Georg, O. Jonsson, V. Fedoseyev, V. Mishin, M. Seliverstov, J. Van Roosbroeck, S. Gheysen, M. Huyse, K. Kruglov, G. Neyens, and P. Van Duppen. Magnetic Moments of ^{68}Cu^{g,m} and ^{70}Cu^{g,m1,m2} Nuclei Measured by In-Source Laser Spectroscopy. *Physical Review C*, 65(2):024315, 2002.

[35] S. Liberman, J. Pinard, H. T. Duong, P. Juncar, P. Pillet, J.-L. Vialle, P. Jacquinot, F. Touchard, S. Buttgenbach, C. Thibault, M. de Saint-Simon, R. Klapisch, A. Pesnelle, and G. Huber. Laser Optical Spectroscopy on Francium D_2 Resonance Line. *Physical Review A*, 22(6):2732–2737, 1980.

[36] P. Van Duppen. *The Euroschool Lectures on Physics With Exotic Beams, Vol. II: Isotope Separation On Line and Post Acceleration*, volume 77. Springer-Verlag, 2006.

[37] E. Kugler, D. Fiander, B. Jonson, H. Haas, A. Przewloka, H. L. Ravn, and D. J. Simon. The New CERN-ISOLDE On-Line Mass-Separator Facility at the PS-Booster. *Nuclear Instruments and Methods in Physics Research Section B: Beam Interactions with Materials and Atoms*, 70:41–49, 1992.

[38] I. P. Aliseda. *New Developments on Preparation of Cooled and Bunched Radioactive Ion Beams at ISOL-Facilities: The ISCOOL Project and the Rotating Wall Cooling*. Phd thesis, Universitat Politècnica de Catalunya, 2006.

[39] H. Franberg, P. Delahaye, J. Billowes, K. Blaum, R. Catherall, F. Duval, O. Gianfrancesco, T. Giles, A. Jokinen, M. Lindroos, D. Lunney, E. Mane, and I. Podadera. Off-Line Commissioning of the ISOLDE Cooler. *Nuclear Instruments and Methods in Physics Research Section B: Beam Interactions with Materials and Atoms*, 266(19-20):4502–4504, 2008.

[40] E. Mane, J. Billowes, K. Blaum, P. Campbell, B. Cheal, P. Delahaye, K. T. Flanagan, D. H. Forest, H. Franberg, C. Geppert, T. Giles, A. Jokinen, M. Kowalska, R. Neugart, G. Neyens, W. Nortershauser, I. Podadera, G. Tungate, P. Vingerhoets, and D. T. Yordanov. An Ion Cooler-Buncher for High-Sensitivity Collinear Laser Spectroscopy at ISOLDE. *The European Physical Journal A*, 42(3):503–507, 2009.

[41] T. J. Procter, H. Aghaei-Khozani, J. Billowes, M. L. Bissell, F. Le Blanc, B. Cheal, T. E. Cocolios, K. T. Flanagan, H. Hori, T. Kobayashi, D. Lunney, K. M. Lynch, B. A. Marsh, G. Neyens, J. Papuga, M. M. Rajabali, S. Rothe, G. Simpson, A. J. Smith, H. H. Stroke, W. Vanderheijden, and K. Wendt. Development of the CRIS (Collinear Resonance Ionisation Spectroscopy) beam line. *Journal of Physics: Conference Series*, 381:012070, 2012.

[42] J. L. Wiza. Microchannel Plate Detectors. *Nuclear Instruments and Methods*, 162(1-3):587–601, 1979.

[43] M. M. Rajabali, K. M. Lynch, T. E. Cocolios, J. Billowes, M. L. Bissell, S. De Schepper, K. Dewolf, K.T. Flanagan, F. Le Blanc, B. A. Marsh, P. J. R. Mason, I. Matea, G. Neyens, J. Papuga, T. J. Procter, S. Rothe, G. S. Simpson, A. J. Smith, H. H. Stroke, D. Verney, P. M. Walker, K. Wendt, and R. T. Wood. A Dedicated Decay-Spectroscopy Station for the Collinear Resonance Ionization Experiment at ISOLDE. *Nuclear Instruments and Methods in Physics Research Section A: Accelerators, Spectrometers, Detectors and Associated Equipment*, 707:35–39, 2013.

[44] G. Racah. Theory of Complex Spectra. II. *Physical Review*, 62:438–462, 1942.

[45] A. Coc, C. Thibault, F. Touchard, H. T. Duong, P. Juncar, S. Liberman, J. Pinard, J. Lermé, J. L. Vialle, S. Buttgenbach, A. C. Mueller, A. Pesnelle, and ISOLDE Collaboration. Hyperfine Structures and Isotope Shifts of $^{207\text{-}213,220\text{-}228}$Fr; Possible Evidence of Octupolar Deformation. *Physics Letters*, 163(1):1–5, 1985.

[46] H. T. Duong, P. Juncar, S. Liberman, A. C. Mueller, R. Neugart, E. W. Otten, B. Peusse, J. Pinard, H. H. Stroke, C. Thibault, F. Touchard, J. L. Vialle, K. Wendt, and ISOLDE Collaboration. First Observation of the Blue Optical Lines of Francium. *Europhysics Letters*, 3(2):175–182, 1987.

[47] J. S. Grossman, L. A. Orozco, M. R. Pearson, J. E. Simsarian, G. D. Sprouse, and W. Z. Zhao. Hyperfine Anomaly Measurements in Francium Isotopes and the Radial Distribution of Neutrons. *Physical Review Letters*, 83(5):935–938, 1999.

[48] V. A. Dzuba, W. R. Johnson, and M. S. Safronova. Calculation of Isotope Shifts for Cesium and Francium. *Physical Review A*, 72(2):8, 2005.

[49] C. Ekstrom, L. Robertsson, and A. Rosen. Nuclear and Electronic g-Factors of \superscript{211}Fr, Nuclear Ground-State Spin of \superscript{207}Fr and the Nuclear Single-Particle Structure in the Range \superscript{207-228}Fr. *Physica Scripta*, 34:624–633, 1986.

[50] Y. Ting and D. Williams. Nuclear Gyromagnetic Ratios. IV. *Physical Review*, 89(3):595, 1953.

[51] R. Neugart, H. H. Stroke, S. A. Ahmad, H. T. Duong, H. L. Ravn, and K. Wendt. Nuclear Magnetic Moment of ^{207}Tl. *Physical review letters*, 55(15):1559–1562, 1985.

[52] J Wouters, N Severijns, J Vanhaverbeke, and L Vanneste. Magnetic Moments of Po Isotopes and the Quenching of Nuclear Magnetism in the \superscript{208}Pb region. *Journal of Physics G Nuclear and Particle Physics*, 17:1673–1682, 1991.

[53] T. E. Cocolios, W. Dexters, M. D. Seliverstov, a. N. Andreyev, S. Antalic, a. E. Barzakh, B. Bastin, J. Büscher, I. G. Darby, D. V. Fedorov, V. N. Fedosseyev, K. T. Flanagan, S. Franchoo, S. Fritzsche, G. Huber, M. Huyse, M. Keupers, U. Köster, Yu. Kudryavtsev, E. Mané, B. a. Marsh, P. L. Molkanov, R. D. Page, a. M. Sjoedin, I. Stefan, J. Van de Walle, P. Van Duppen, M. Venhart, S. G. Zemlyanoy, M. Bender, and P.-H. Heenen. Early Onset of Ground State Deformation in Neutron Deficient Polonium Isotopes. *Physical Review Letters*, 106(5):052503, 2011.

Instituut voor Kern- en Stralingsfysica
Celestijnenlaan 200d - bus 2418
3001 Heverlee, BELGIË
tel. + 32 16 32 72 63
fax + 32 16 32 79 85
http://fys.kuleuven.be/iks